Second-year modeling project - École Nationale de la Météorologie

Data assimilation for wildfire spread forecasting: comparison of rate of spread models

Marion RIVERAIN, Valentine CHATEL, Céline VARGEL

Sophie RICCI, CERFACS/SUC-CNRS URA 1875
Mélanie ROCHOUX, Environment Canada
Arnaud TROUVÉ, University of Maryland
Bernard ICHÉ, ENM

Credit: Laurent JOEL - Cemagref

January-February 2015

Remerciements

Nos premiers remerciements vont à Sophie Ricci et Mélanie Rochoux, pour nous avoir ouvert les portes de la recherche ainsi que pour nous avoir accompagnées pendant ces 6 semaines de travail. Votre présence a été constante tout au long de notre projet, même de l'autre côté de l'Atlantique. Vous avez toujours été disponibles pour répondre à nos questions, nous conseiller, nous aider, ainsi que pour relire de nombreuses fois notre rapport, tout en nous encourageant continuellement.

Nous tenons également à remercier Arnaud Trouvé pour le travail préparatoire, effectué avec Sophie et Mélanie, afin de nous permettre d'effectuer notre projet. Nous voulons également remercier Cong Zhang pour ces précieuses informations et données sur l'expérience FireFlux ainsi qu'Anthony Thevenin et Isabelle d'Ast pour leur soutien informatique afin de pouvoir faire tourner le modèle FireFly.

Nous remercions toute l'équipe Global Change du CERFACS pour son accueil chaleureux au sein de l'équipe.

Résumé

La prévision en temps réel d'un feu de forêt qui se propage reste une tâche difficile, car ce problème implique à la fois de multiples processus physiques et de multiples échelles. La vitesse de propagation des feux de forêt (VDP) est déterminée par des interactions complexes entre la pyrolyse de la biomasse et la dynamique de la combustion et de l'atmosphère, qui ont lieu aux échelles végétales, topographiques et météorologiques. Comme les incendies se présentent en général sous forme de fronts à des échelles régionales, les simulateurs opérationnels actuels les représentent sous forme d'un front se propageant à une VDP tirée d'un modèle semi-empirique. Dans ce modèle, la VDP est traitée comme un fonction simplifiée des paramètres de végétation (humidité relative), des propriétés topologiques et météorologiques (force et direction du vent près du sol). Pour que la simulation de la propagation soit juste, les incertitudes sur le modèle de VDP doivent être réduites. Les récents progrès en matière de télédétection proposent de nouvelles méthodes pour surveiller la position du front de flamme, une approche prometteuse pour surmonter les difficultés rencontrées dans la modélisation de la propagation des feux de forêt étant de combiner la modélisation du feu et la télédétection, en utilisant l'assimilation de données.

La possibilité de compléter les simulations avec des observations à haute résolution est apparue seulement dans les dix dernières années et reste encore rarement disponible en temps réel pour de nouvelles applications environnementales telles que les inondations ou la prévision de la propagation des incendies. Dans le domaine de recherche sur le feu, des travaux importants ont été réalisés en matière d'assimilation de données avec un modèle simple de propagation (FireFly), montrant que l'assimilation de la position du front donne une meilleure estimation des paramètres d'entrée (données végétales et météorologiques) ainsi qu'une correction anisotropique de la position du front de flamme à un instant donné. La validation de FireFly était jusque là limitée à des expériences en laboratoires et à des feux de prairie contrôlés à échelle réduite.

Pour pouvoir passer en opérationnel, l'assimilation de données doit être testée sur des feux plus réalistes ayant lieu à des échelles régionales. Pour ce faire, le présent projet de recherche, mené conjointement par le CERFACS et l'université du Maryland cherche à évaluer la performance de FireFly sur l'expérience référence de feu contrôlé FireFlux (30 ha) à travers la comparaison avec les résultats obtenus avec le couplage de modèles feu/atmosphère ForeFire/MésoNH. Tout d'abord, le présent projet modélisation propose une comparaison des modèles de VDP utilisés dans FireFly (Rothermel) et ForeFire (Balbi). Cette comparaison est faite sur une configuration simplifiée (étude 0D) et dans le cadre du modèle FireFly (propagation sur une surface 2D).

Les résultats montrent que les deux modèles sont en accord sur la direction de propagation du front de feu. Cependant, il semble que le modèle de Balbi propose une vitesse de propagation supérieure à celle proposée par le modèle de Rothermel sur les cas testés.

Abstract

Real-time predictions of a propagating wildfire remain a challenging task because the problem involves both multi-physics and multi-scales. The propagating speed of wildfires, also called the rate of spread (ROS), is determined by complex interactions between biomass pyrolysis, combustion and atmospheric dynamics occurring at vegetation, topographical and meteorological scales. As a wildfire generally features a front-like geometry at regional scales, current operational simulators represent it as a propagating front at a ROS based on a semi-empirical model formulation. In this formulation, the ROS is treated as a simplified parametric function of vegetation (e.g., moisture content), topographical and meteorological (e.g., near-surface wind speed and direction) properties. For the fire spread simulation to be predictive, the uncertainty on the ROS model should be reduced. As recent progress made in remote sensing technology provides new ways to monitor the fire front position, a promising approach to overcome the difficulties found in wildfire spread simulations is to integrate fire modeling and fire sensing technologies using data assimilation.

The capacity of feeding simulations with measurements at high resolution has only emerged over the past decade and is still rarely available in real-time for new environmental applications such as flood or wildfire spread forecasting. In the fire research field, major work was recently done in the field of data assimilation with a simplified propagation model (FireFly), showing that the assimilation of fire front positions provides more accurate estimation of input data (meteorological and vegetation characteristics) as well as an anisotropic correction of the fire front position at a given time. The evaluation of FireFly was so far limited to synthetic experiments and to a reduced-scale controlled grassland burning.

In order to move towards operational framework, the data assimilation strategy needs to be tested against more realistic wildfire events evolving at regional scales. For this purpose, the current research project led jointly at CERFACS and the University of Maryland aims at evaluating the performance of FireFly on the well-known controlled fire experiment FireFlux (30 ha) through the comparison with the simulation results obtained with the ForeFire/MésoNH fire–atmosphere coupled solver. As a preliminary step, the present ENM modeling project provides a comparison of the ROS semi-empirical formulations used in FireFly (Rothermel) and ForeFire (Balbi). This comparison is performed on a simplified configuration (0-D study) and in the framework of the FireFly simulator (2-D surface propagation).

The results indicate that both model agree with each other. They propagated the fireline in the same direction but the ROS is faster for Balbi's model in the test cases presented in this work.

Contents

1 Introduction

As second-year students of the French National school of Meteorology (Ecole Nationale de la Météorologie – ENM), we have the opportunity to carry out a 5-week internship related to modeling in a research laboratory. Our work group consists of 3 people under the supervision of Sophie RICCI, Mélanie ROCHOUX and Arnaud TROUVÉ. We have chosen the project proposed by CERFACS (Centre Européen de Recherche et de Formation Avancée en Calcul Scientifique) related to data assimilation for wildfire spread forecasting. It is indeed an opportunity to discover a new field of study, wilfire spread, yet closely related to meteorology (e.g., near-surface wind condition, plume dynamics and chemistry).

1.1 Multi-scale multi-physics problem

Wildfires, also referred to as wildland, forest or bush fires, constitute a global issue, affecting almost all climates, tropical belts as much as boreal ecosystems. Real-time prediction of the direction and speed of a propagating wildfire has been identified as a valuable research objective with direct applications in both fire management and fire emergency response. The dynamics of wildfires are characterized by multi-scale interactions. These interactions occur between biomass dynamics and pyrolysis, combustion and flow dynamics as well as atmospheric dynamics and chemistry. As illustrated in Fig. 1, these interactions occur at different scales (Viegas, 2011): vegetation scales (biomass fuel), flame scales (combustion and heat transfer processes), topographical scales (terrain and vegetation boundary layer) and meteorological micro- and mesoscales (atmospheric conditions).

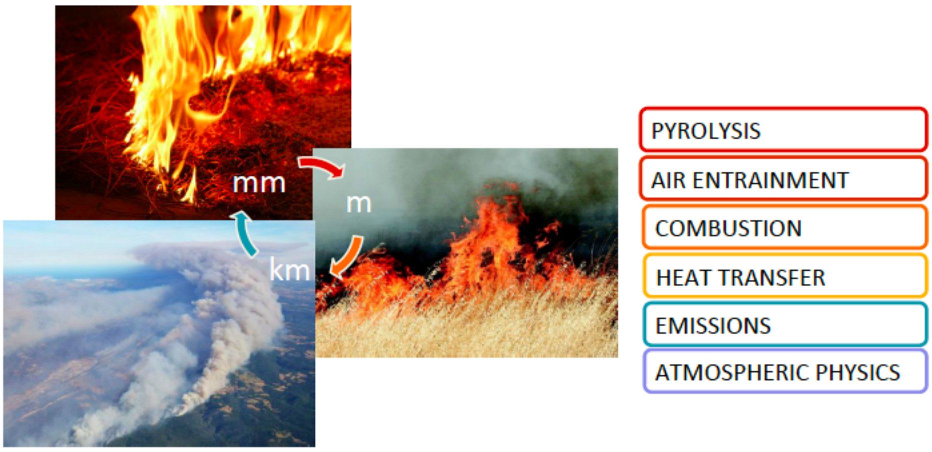

Figure 1: Schematic of multi-scale multi-physics processes underlying wildfires. Credits: Rochoux (2014a).

To start, a fire requires an external heat source (e.g., human-induced ignition, thunderstorm lightning). Once being ignited, thanks to chemicals reactions between oxygen and flammable gases that are released by the pre-heated vegetation (e.g., CH_4, CO, H_2), the fire can self-sustain. Fons (1946) suggested that wildfire propagation can be regarded as a succession of ignitions inducing the displacement of the pyrolysis zone (and thereby of the flame zone) towards the unburnt region. Viegas (1998) distinguishes two main modes of propagation shown in Fig. 2, namely flaming combustion and smoldering combustion. Flaming combustion corresponds to the case when

Figure 2: Snapshot of undergrowth burning separating two modes of biomass combustion: (1) the flaming mode in grass (the flame is 10 mm tall); and (2) the smoldering mode in organic soils. Credits: Ashton et al. (2007).

combustion-released processes produce a flame, the visible part of the fire illustrated in Fig. 2. Smoldering combustion, also named ground fires, occurs through surface and sub-surface organic layers of the forest ground, at low temperatures and usually without any flame (Ashton et al., 2007; Hadden et al., 2013).

Fire self-sustaining mechanism and biomass fuel thermal degradation can be described as a series of four main stages, detailed below (Williams, 1982) and presented in Fig. 3:

(1) **Flame-induced convection and radiation heat transfer.** The combustion zone, where combustion kinetic reactions occur, releases a large amount of heat through convection and radiation. In particular, the vegetation ahead of the combustion zone (in the pre-heated zone) receives a significant external heat flux from the flame and therefore, its temperature increases. The magnitude of this external heat flux decreases with distance from the flame.

(2) **Moisture evaporation.** This constitutes the primary stage of the vegetation thermal degradation: the moisture contained in the porous vegetation of the pre-heated zone evaporates, which breaks the chemical bonds within the porous organic material and modifies its composition.

(3) **Pyrolysis gas release.** The temperature of the porous vegetation continues to rise and above a certain threshold temperature (typically, 450-650 K), the solid phase of the vegetation starts to release flammable gas compounds (e.g., $\mathrm{CH_4}$, CO, $\mathrm{H_2}$) that are convected through the vegetation layer towards the flame front. This entrainment is due to buoyancy effects. Since the burnt gases produced by the flame have a significantly lower density than ambient air (due to temperature discrepancies), they rise by convection and generate air streams (referred to as air entrainment), which push pyrolysis gas reactants towards the flame. This constitutes the pyrolysis stage, which can be regarded as a phase transformation (i.e., from solid-phase to gas-phase) within the porous vegetation.

(4) **Onset of combustion kinetic reactions.** Once the flammable gases released during the pyrolysis process are in contact with oxygen, oxidation reactions can proceed if the gas temperature is sufficiently high. A flame develops above the

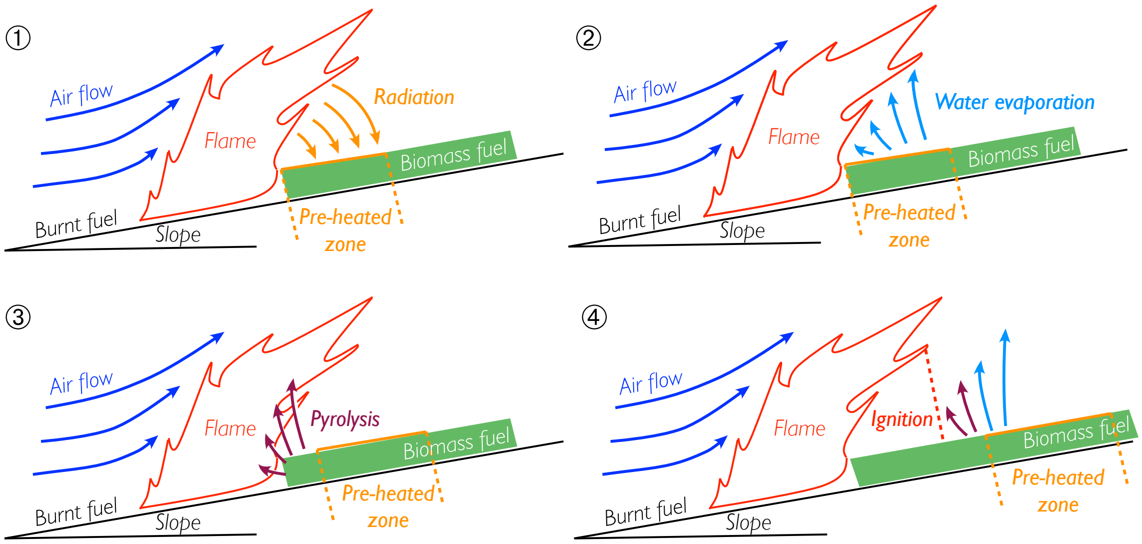

Figure 3: Successive stages leading to wildfire spread (schematic restricted to the flaming mode of combustion). (1) Biomass preheating, (2) Water evaporation, (3) Pyrolysis (evaporation of flammable gas compounds), (4) Combustion. Credits: Rochoux (2014a).

previously-mentioned pre-heated zone and in turn, releases heat towards the vegetation located ahead of the flaming front. This induces the displacement of the flame towards the unburnt vegetation. Note that the temperature at which pyrolysis gases are released (nearly 600 K) commonly defines the interface between the combustion zone and the pre-heated zone.

1.2 Wildfire spread modeling

During the past two decades, computer-based wildfire spread modeling emerged. Due to its front-like topology at regional scales, a wildfire is generally considered as a propagating interface from the burnt area to the unburnt vegetation. This propagating interface is referred to as the fire front or fireline.

The rate of displacement of the fire front is named rate of spread (ROS). A fireline travels at a ROS that results from complex interactions between biomass pyrolysis, combustion and flow dynamics as well as atmospheric dynamics that are still not well understood. Different modeling approaches have been proposed to cope with the complexity of wildfire spread. On the one hand, the physics-based approach intends to explicitly resolve interactions between the vegetation and the flame as well as between the flame and the atmospheric dynamics (Hanson et al., 2000); it simulates the fundamental chemical and physical processes within and above the vegetation by explicitly solving for mass, momentum and energy balance equations (Grishin, 1997; Larini et al., 1998; Linn et al., 2002; Morvan and Dupuy, 2004; Porterie et al., 2005). Due to its prohibitive computational cost, this approach is limited to numerical simulations performed at flame scales. That is why current operational wildfire spread simulators adopt a regional-scale viewpoint (i.e., a viewpoint that considers scales ranging from a few tens of meters up to several kilometers). These computer-based systems aim at forecasting the behavior of the fire front for a given set of environmental conditions and ignition location, using a parameterization of the ROS model. There are different ways to estimate the ROS (e.g., Rothermel 1972; Balbi et al. 2009). In this project, the selected approach relies on a semi-empirical formulation of the ROS, an intermediate between physics-based and empirical modeling. It consists in (1) formulating the ROS using an energy balance equation (applied to the unburnt vegetation located in the pre-heated zone); and (2) calibrating the resulting model parameters using experimental data.

1.3 Modeling project

CERFACS has been working on the issue of data-driven wildfire spread forecasting over the past 5 years. Mélanie Rochoux worked on the development of a prototype data-driven wildfire spread simulator named FireFly during her PhD (2010–2014). This prototype simulator relies on a fire spread model combining a simplified semi-empirical ROS model and an Eulerian front-tracking solver, which sequentially assimilates the location of the fire front in order to provide more accurate estimation of the input data (near-surface wind, biomass moisture content, etc.). The data assimilation algorithm is based on an ensemble Kalman Filter (EnKF). This EnKF algorithm either relies on a parameter estimation approach in which input parameters of the ROS are estimated, or on a state estimation approach in which the location of the fire front is directly estimated. In the latter, the two-dimensional coordinates of the front markers along the discretized fire front are corrected, thus providing a more reliable initial condition for further model time-integration. The EnKF-based prototype has shown its good ability to track a small-scale controlled grassland fire and to retrieve a more physical ROS along the fireline.

ENM students, Clément Doche in 2012 as well as Caroline Allouache, Mickaël Durand, Maxime Taillardat for the 2013 ENM modeling internship, joined the project to apply the data assimilation strategy to a new front-tracking simulator named ForeFire, which is compatible with operational applications and able to handle complex vegetation and wind input data settings. ForeFire has been coupled with MésoNH within the IDEA (Incendies, de la Dynamique aux Emissions Atmosphériques) project (2010–2013) funded by the ANR (Agence Nationale de la Recherche). These studies were limited to synthetic experiments, yet preliminary results have demonstrated promising potential to apply the newly-developed data assimilation strategy to a more operationally-oriented simulator and thereby to real-case wildfire events.

The objective of this project is to compare two semi-empirical ROS models, Balbi's model (Balbi et al., 2009) and Rothermel's model (Rothermel, 1972) in Balbi's model, the ROS is estimated with more sub-models and less empirical parameters. In order to compare the two model formulations, a simplified Matlab model is first used to perform a 0-D sensitivity study and then, FireFly simulations are performed on a well-known controlled fire experiment named FireFlux, which is a 0.63 km^2 experimental plan burn of tall grass instrumented with wind profilers and thermocouples (Clements, 2007; Kochanski et al., 2013; Filippi et al., 2013). The general organization of the project's work is described in appendix A and to better understand the different variable's names, appendix D presents name's french translation.

The outline of this report is as follows. First, Section 2 presents a physical approach to wildfire spread. Then, Section 3 briefly describes the tools and experimental settings for the project. Section 4 presents the comparison between Balbi's (Balbi et al., 2009) and Rothermel's (Rothermel, 1972) ROS approach using the simplified Matlab model and FireFly.

2 A physical approach to wildfire spread

2.1 Rothermel's rate of spread model

The Rothermel's ROS model is a widely known semi-empirical model developed in the 1970s at the US Forest Service (Rothermel, 1972), based on one-dimensional wind-tunnel experiments and on the derivation of the energy conservation equation by Fons (1946) and Frandsen (1971). The Rothermel's model evaluates the local ROS given environmental conditions (near-surface wind conditions, biomass fuel moisture content, terrain topography, etc.).

2.1.1 Input parameters

The one-dimensional formulation of the ROS (noted Γ [m/s]) proposed by Rothermel (1972) requires 11 input parameters described in Table 1 such that:

$$\Gamma = \Gamma\Big(\delta_v, \beta_v, M_v, M_{v,ext}, \Sigma_v, m''_v, \rho_p, \Delta h_c, s_t, s_e, u_w, \alpha_{sl}\Big). \tag{1}$$

Some parameters are assumed to be independent of the biomass fuel type and have fixed value referred to as *nominal value* in Table 1 (e.g., fuel moisture at extinction $M_{v,ext}$, fuel particle mass density ρ_p, fuel low heat of combustion Δh_c, etc.); the other are based on field-based controlled fire experiments.

Name	**Symbol**	**Unit**	**Nominal value**
Fuel depth (vertical thickness of the vegetation layer)	δ_v	m	-
Fuel packing ratio (Fraction of fuel bed occupied by fuel particles)	β_v	%	-
Fuel moisture (mass of water divided by mass of dry vegetation)	M_v	%	-
Fuel moisture at extinction (Minimal value of the moisture content preventing the fuel from burning)	$M_{v,ext}$	%	30.0
Fuel particle surface-to-volume ratio	Σ_v	1/m	-
Fuel loading	m''_v	kg/m^2	-
Fuel particle mass density	ρ_p	kg/m^3	512.4
Fuel low heat of combustion	Δh_c	J/kg	18.608×10^6
Fuel particle total mineral content	s_t	%	5.55
Fuel particle effective mineral content	s_e	%	1.0
Wind velocity at mid-flame height (projected onto horizontal plane)	u_w	m/s	-
Terrain slope angle	α_{sl}	°	-

Table 1: Input parameters of the Rothermel's ROS model. Parameters with specified nominal values correspond to properties shared by the different biomass fuel species in Rothermel's fuel database.

2.1.2 Formulation

From a modeling point of view, the ROS is defined as the ratio between the flame-induced heat flux and the heat required for biomass ignition (see Eq. 2). Γ corresponds to the following energy ratio:

$$\Gamma = \frac{I_p}{\rho_b\, \varepsilon\, Q_{ig}}, \tag{2}$$

with:

- ▷ I_p [J/m^2/s] the propagating heat flux received by the unburnt vegetation;
- ▷ $\rho_b\, \varepsilon$ [kg/m^3] the effective fuel density (i.e., the amount of vegetation per unit volume of the fuel bed raised to ignition ahead of the advancing fire);
- ▷ Q_{ig} [J/kg] the heat of pre-ignition (i.e., the heat required to bring a unit weight of fuel to ignition).

The propagating heat flux (I_p) represents the total heat transfer when summing the contributions of slope and wind on the fire propagation (see Fig. 4). Rothermel's model introduces the concept of the no-wind no-slope propagating flux noted $I_{p,0}$, which represents the minimal value for the propagating heat flux achieved for no-wind and flat terrain conditions. Then, the wind effect ($I_{p,0} \times \phi_w^*$) and the slope effect ($I_{p,0} \times \phi_{sl}^*$) are added to ($I_{p,0}$) as follows:

$$I_p = I_{p,0}\left(1 + \phi_w^* + \phi_{sl}^*\right), \tag{3}$$

with ϕ_w^* and ϕ_{sl}^* the wind and slope correction coefficients that are parameterized using statistics derived from wind-tunnel experiments. Through this formulation, the Rothermel-based ROS increases with the wind velocity and/or with the terrain slope. Indeed, in case of wind-aided or up-slope propagation, a faster wildfire propagation is due to the higher flame tilt angle towards the unburnt vegetation, which enhances radiation and convection heat transfer, and which accelerates biomass thermal degradation. Note that the wind and slope contributions are only additive in Eq. (3).

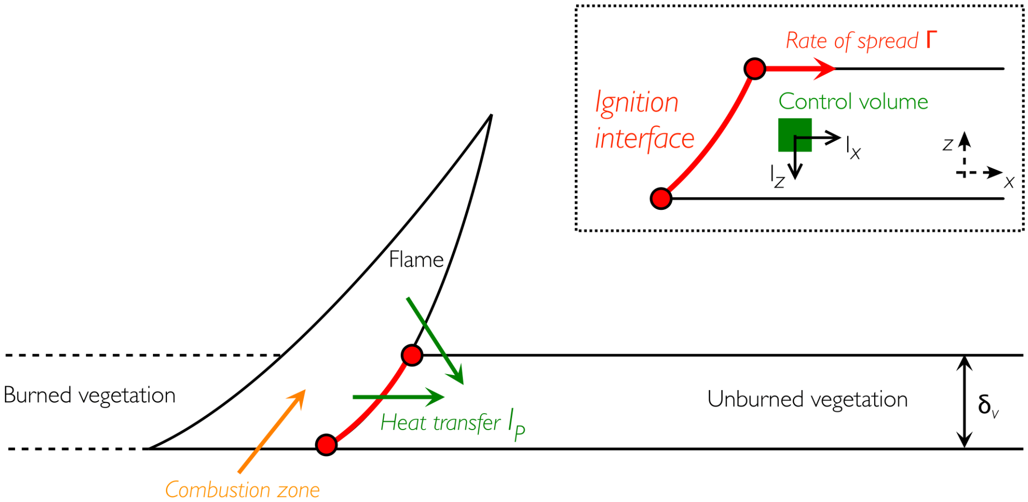

Figure 4: Schematic of the wildfire spread mechanism with I_p the propagating heat flux derived from an energy budget in a control volume of the vegetation ahead of the flame. Credit: Rochoux (2014a).

In the ROS model due to Rothermel (1972), the no-wind no-slope propagating heat flux ($I_{p,0}$) is assumed proportional to the flame heat release rate I_r (the proportionality coefficient is noted χ). Thus, the Rothermel-based ROS Γ is defined as follows:

$$\Gamma = \Gamma_0 \left(1 + \phi_w^* + \phi_{sl}^*\right) = \frac{\chi I_r}{\rho_b \, \varepsilon \, Q_{ig}} \left(1 + \phi_w^* + \phi_{sl}^*\right), \tag{4}$$

with Γ_0 the no-wind no-slope ROS, corresponding to the minimal value of the ROS achieved for no-wind and flat terrain conditions.

2.1.3 Sub-models

Rothermel's ROS sub-models give specific information about the combustion and biomass thermal degradation processes involved in Eq. (4), such as the reaction intensity I_r and the optimum reaction velocity γ. The explicit formulation for the representation of these processes is provided in the following.

▷ Reaction intensity I_r [W/m^2]

$$I_r = \gamma \, m_n'' \, \Delta h_c \, n_m \, n_s. \tag{5}$$

▷ Optimum reaction velocity γ [s^{-1}]

$$\gamma = \gamma_{\max} \left(\frac{\beta_v}{\beta_{v,op}}\right)^A \exp\left[A \left(1 - \frac{\beta_v}{\beta_{v,op}}\right)\right], \tag{6}$$

with $A = \left(4.774 \, (\Sigma_v)^{0.1} - 7.27\right)^{-1}$.

▷ Maximum reaction velocity $\gamma_{\max}$ [s^{-1}]

$$\gamma_{\max} = \Sigma_v^{1.5} \left(495 + 0.0594 \, \Sigma_v^{1.5}\right)^{-1}. \tag{7}$$

▷ Optimum packing ratio $\beta_{v,op}$ [-]

$$\beta_{v,op} = 3.348 \, \Sigma_v^{-0.8189}. \tag{8}$$

▷ Bulk mass density ρ_b [kg/m^3]

$$\rho_b = \beta_v \, \rho_p. \tag{9}$$

▷ Fuel loading m_v'' [kg/m^2]

$$m_v'' = \rho_b \, \delta_v. \tag{10}$$

▷ Net fuel loading m_n'' [kg/m^2]

$$m_n'' = \frac{m_v''}{1 + s_t}. \tag{11}$$

▷ Moisture damping coefficient n_m [-]

$$n_m = 1 - 2.59 \left(\frac{M_v}{M_{v,ext}}\right) + 5.11 \left(\frac{M_v}{M_{v,ext}}\right)^2 - 3.52 \left(\frac{M_v}{M_{v,ext}}\right)^3. \tag{12}$$

▷ Mineral damping coefficient n_s [-]

$$n_s = 0.174 \, s_e^{-0.19}. \tag{13}$$

▷ Propagating heat flux χ [-]

$$\chi = (192 + 0.2595\,\Sigma_v)^{-1}\ \exp\left[\left(0.792 + 0.681\,\Sigma_v^{0.5}\right)(\beta_v + 0.1)\right]. \tag{14}$$

▷ Wind correction coefficient ϕ_w^* [-]

$$\phi_w^* = C\,u_w^B \left(\frac{\beta_v}{\beta_{v,op}}\right)^{-E}, \tag{15}$$

with:

$$\begin{aligned} C &= 7.47\ \exp\left[-0.133\,\Sigma_v^{0.55}\right], \\ B &= 0.02526\,\Sigma_v^{0.54}, \\ E &= 0.715\ \exp\left[-3.59 \times 10^{-4}\,\Sigma_v\right]. \end{aligned} \tag{16}$$

▷ Slope correction coefficient ϕ_{sl}^* [-]

$$\phi_{sl}^* = 5.275\,\beta_v^{-0.3}\ (\tan\alpha_{sl})^2\,. \tag{17}$$

▷ Effective heating number ε [-]

$$\varepsilon = \exp\left[-\frac{138}{\Sigma_v}\right]. \tag{18}$$

▷ Heat of pre-ignition Q_{ig} [J/kg]

$$Q_{ig} = 250 + 1.116\,M_v. \tag{19}$$

2.2 Balbi's rate of spread model

2.2.1 Assumptions

There are alternative semi-empirical ROS formulations in the literature (Sullivan, 2009; Cheney et al., 1998; Balbi et al., 2009). This project particularly focuses on the formulation provided by Balbi et al. (2009), based on three balance equations that stem from mass, energy and momentum budget (instead of the stand-alone energy budget in the Rothermel's formulation, see Section 2.1). Furthermore, two sub-models further detail the physical representation of the fire propagation in Balbi's formulation, a radiation sub-model estimating the amount of energy transferred to the vegetation ahead of the flame front on the one hand and a preheating sub-model describing the radiative effects within the vegetation layer ahead of the fire front on the other hand. The assumptions listed below are introduced, in order to explicit the ROS formulation referred to as the Balbi's model in the following:

(1) The normal cut of the flame volume is assumed to have on average a triangular shape, which is consistent with observed results and convenient to reduce the number of geometrical parameters (represented in Fig. 5) required for the description of heat and mass fluxes.

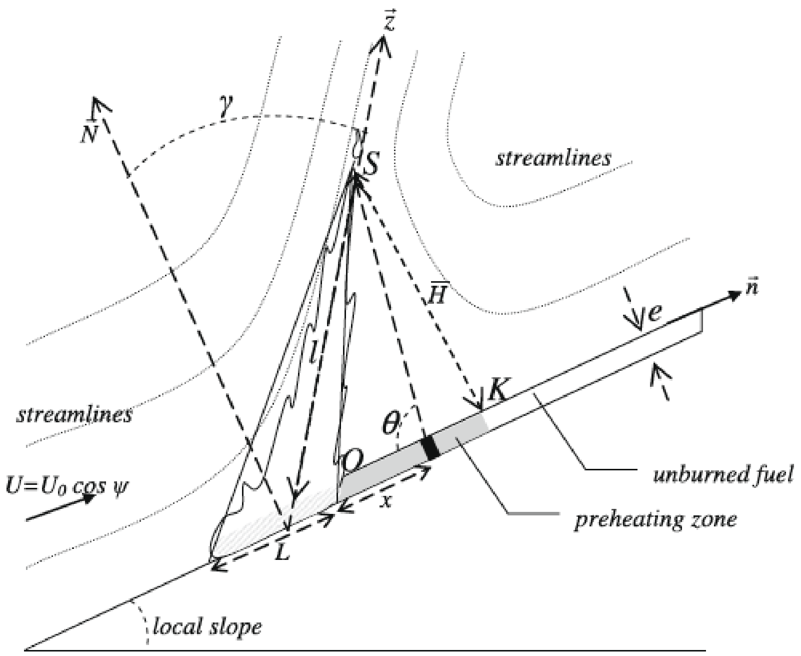

Figure 5: Flame profile along the normal direction **n**. Note that the tilt angle noted γ on this scheme is designed in this report by α_{fr}. Credit: Balbi et al. (2009).

(2) Thermal radiation is considered as the dominating heat transfer mechanism in the pre-heated vegetation zone under the flame (as long as the flame is not too tilted toward the ground, in which case convection becomes the dominating heat transfer mechanism). Convection plays an essential role beyond the zone over which the flame is projected because the flame-induced flow of fresh air towards the flame has a convective cooling effect on the vegetation. In this context, the flame is supposed to behave as a radiant plane.

(3) The amount of energy emitted by radiation, the radiation factor (noted χ_{rad}) is a decreasing function of the surface-to-volume ratio of the flame (Σ_v) because if the volume of the flame decreases (with a constant flame surface), the proportion of energy emitted by radiation to the overall released energy must also decrease.

(4) Gases are considered to be perfect and the thermodynamic transformations are isobaric (because of the validity of the low-Mach-number approximation in natural fires). The flame can be described with a uniformly-distributed average temperature T_{fr}.

(5) The combustion chemical reactions are reduced to a single reaction occurring at stoichiometry: $\mathrm{C} + \mathrm{O_2} \rightarrow \mathrm{CO_2}$. The associated stoichiometric coefficient is denoted by s and is set to 9 (meaning that 1 kg of pyrolysis gases is completely consumed for 9 kg of air).

(6) The vegetation is assumed to be made of solid particles of homogeneous properties in terms of moisture content M_v, surface-to-volume ratio Σ_v, temperature of the vegetation T_v, etc..

(7) A constant mass loss rate (denoted by $\dot{m}_v''$) is supposed for the vegetation as soon as the gas temperature reaches the assumed biomass ignition temperature T_{ign}.

(8) For every point close to the flame front, the latter is considered as its tangent plane of infinite length and the height of this plane is equal to the flame length (denoted by l in Fig 5).

(9) The radiant plane heats the unburnt fuel only under the flame because the convective column of hot gases of the flame prevents the cooling airflow induced by the convection to flow under the flame.

2.2.2 Input parameters

In Balbi's ROS formulation, 8 parameters are common to Rothermel's model and 8 new parameters are added in order to represent more physical processes and to obtain close-formed additional equations. The common parameters are the following: the fuel loading (m_v''), the fuel layer depth (δ_v), the fuel particle surface-to-volume ratio (Σ_v), the fuel low heat of combustion (Δh_c), the fuel particle mass density (ρ_p), the fuel moisture content (M_v), the wind velocity at mid-flame height (u_w) and the terrain slope angle (α_{sl}).

The additional parameters related to radiation and convection heat transfer are listed below:

- ε_{fr} [-] the flame emissivity;
- ε_v [-] the vegetation emissivity;
- χ_{rad} [-] the radiation fraction: ratio of the radiation heat to the total heat received by the vegetation;

- ▷ u_b [m/s] the buoyancy velocity: upward velocity of the gas reactants for no-wind no-slope conditions;
- ▷ Δh_v [J/kg^3] the moisture evaporation enthalpy: amount of energy required to evaporate moisture within the vegetation;
- ▷ $c_{p,v}$ [J/kg/K] the fuel calorific capacity: specific heat for vegetation at constant pressure;
- ▷ T_{ign} [K] the fuel ignition temperature;
- ▷ T_{air} [K] the ambient air temperature.

2.2.3 Governing equations

The main equations contained in Balbi's ROS formulation are presented below for a fire in the wind and up-slope directions. For more details, refer to Balbi et al. (2009).

Mass budget – Based on the mass balance equation with assumption of a stoichiometric mixture, the buoyant velocity u_b reads:

$$u_b = \frac{2\,\dot{m}_v''(s+1)}{\rho_{fr}\cos(\alpha_{sl})}, \tag{20}$$

with u_{b0} [m/s] the no-slope vertical velocity, s the stoichiometric coefficient, ρ_{fr} $[kg/m^3]$ the flame mass density (assumed constant within the flame region) and $\dot{m}_v''$ $[kg/m^2/s]$ the vegetation mass loss rate.

Momentum budget – The velocity into the flame $\mathbf{u}_{fr}$ results from the sum of the incident wind velocity $\mathbf{u}_w = (u_w \cos\alpha_{sl}, u_w \sin\alpha_{sl})^T$ and the buoyancy velocity $\mathbf{u}_b = (0, u_b)^T$ (due to the heat release). The flame is tilted toward the soil in the direction of the velocity normal component; the flame tilt angle α_{fr} satisfies:

$$\tan\alpha_{fr} = \frac{u_w}{u_b\cos\alpha_{sl}} + \tan\alpha_{sl}. \tag{21}$$

Energy budget – The heat release rate by gaseous combustion along the fireline, (Q_{fr} [W/m]), can be expressed as follows:

$$Q_{fr} = \Delta h_c.\delta_{fr}\dot{m}_v'', \tag{22}$$

with δ_{fr} the fire front depth, Δh_c the fuel low heat of combustion and $\dot{m}_v''$ the mass loss rate, assumed constant in Hyp. (7). Assuming that radiation occurs from the flame region above the fuel and inside the vegetation in the flaming part, and assuming that out of the flame there is a compensation between the cooling-induced airflow and the long-range radiation effect, the radiation heat release rate is given by the term $\chi_{rad}Q_{fr}$. The flame temperature T_{fr} is obtained as follows:

$$T_{fr} = T_{air} + (1-\chi_{rad})\frac{\Delta h_c}{(1+s)c_p}, \tag{23}$$

with c_p the gas calorific capacity, T_{air} the ambient temperature, χ_{rad} the radiation fraction and s the stoichiometric coefficient set to 9 according to Hyp. (5).

Flame height – The equation for the vertical moment applied to the flame reads:

$$\rho_{fr}\frac{\partial u_b}{\partial t} = (\rho_{air}-\rho_{fr})g = \left(\frac{T_{fr}}{T_{air}}-1\right)g = g^*, \tag{24}$$

with g the gravitational constant ($g = 9.81\ m/s^2$), ρ_{fr} the flame gas density, T_{fr} the flame temperature, T_{air} the ambient temperature and u_b the buoyancy velocity. The integration of this equation, with the assumption of a uniformly accelerated motion of hot gases, leads to the following expression of the flame height noted H_{fr}:

$$H_{fr} = \frac{u_b^2}{g\frac{(T_{air}-T_{fr})}{T_{fr}}}. \tag{25}$$

Radiation sub-model – A control volume of the vegetation receives thermal radiation from the flame region above the vegetation (noted R_{fr}) and radiation from the flame part inside the vegetation (noted R_v). The flame region above the vegetation is considered as an infinite gray panel of length l, temperature T, and emissivity ε_{fr}. Thus R_{fr} reads:

$$R_{fr} = \varepsilon_{fr}\sigma_{sb}T_{fr}^4\left(\frac{1-\cos\alpha_{fr,o}}{2}\right), \tag{26}$$

with $\alpha_{fr,o}$ the view angle of the flame, σ_{sb} the Stefan-Boltzmann constant ($5.67 \times 10^{-8}\ W/m^2/K^4$), ε_{fr} the flame emissivity and T_{fr} the flame temperature.

The thermal radiation in the flame part of the vegetation decreases uniformly over the vegetal fuel and is damped at the optical length $\delta_{v,opt}$. At a distance x from the fire front and under the assumption of a gray body, the heat flux R_v is given according to:

$$R_v = \begin{cases} \varepsilon_v\sigma_{sb}T_{fr}^4\left(1-\frac{x}{\delta_{v,opt}}\right)\frac{\delta_v}{\delta_{v,opt}} & \text{if} \quad x \le \delta_{v,opt}, \\ 0 & \text{if} \quad x > \delta_{v,opt}, \end{cases} \tag{27}$$

with ε_v the vegetation emissivity, δ_v the vegetation layer thickness and $\delta_{v,opt}$ the optimal length-scale satisfying:

$$\delta_{v,opt} = \frac{4}{\Sigma_v\beta_v}. \tag{28}$$

with β_v the fuel packing ratio.

Pre-heating sub-model – The thermal budget in a control volume below the flame can be written as follows:

$$m_v''c_p\frac{dT_v}{dt} + \Delta h_m\frac{dm_{H_2O}''}{dt} = R_v + \nu_v R_{fr}, \tag{29}$$

with T_v the mean temperature of the vegetation, Δh_m the moisture evaporation enthalpy, m_{H_2O}'' the vegetation moisture loading, and ν_v the fraction of the flame radiation absorbed by the fuel. According to Hypothesis (2), no convection occurs below the flame. Thus, the fraction of the flame radiation absorbed by the fuel is given by the expression:

$$\nu_v = \min\left(\frac{\delta_v}{\delta_{v,opt}}, 1\right). \tag{30}$$

Using the space variable, following the normal **n** (dx = R dt) and integrating over the interval [0; sup ($\delta, \sin\alpha_{fr}$)] with l as the flame length, this budget reads:

$$Rm_v''\left(c_p\left(T_{ign}-T_{air}\right)+\Delta h_m m_{H_2O}''\right) = \int_0^{\delta} R_v\,\mathrm{d}x + \nu_v\int_0^{l\sin\alpha_{fr}} R_{fr}\,\mathrm{d}x, \tag{31}$$

with:

$$\int_0^{\delta} R_v\,\mathrm{d}x = \frac{1}{2}\varepsilon_v\sigma_{sb}T_v^4\delta_v,\ and: \tag{32}$$

$$\nu_v \int_0^{l \sin \alpha_{fr}} R_{fr}\, dx = \frac{1}{2} \varepsilon_{fr} \sigma_{sb} T_{fr}^4 l \left(1 + \sin \alpha_{fr} - \cos \alpha_{fr}\right). \tag{33}$$

Radiation fraction – According to Hypothesis (3), the radiant fraction χ_{rad} decreases with an increase in the flame surface-to-volume ratio Σ_{fr}. χ_{rad} is expressed by:

$$\chi_{rad} = \frac{\chi_{rad,0}}{1 + \rho_{fr} \Sigma_{fr}}, \tag{34}$$

with $\chi_{rad,0}$ the radiation fraction when the flame surface-to-volume ratio converges to zero. According to the assumption of a thin flame,

$$\Sigma_{fr} = 0.5L \cos \alpha_{fr}. \tag{35}$$

For the high values of α_{fr}, the fraction of the heat release rate due to radiation (χ_{rad}) depends on the ROS Γ as follows:

$$\chi_{rad} = \frac{\chi_{rad,0}}{\left(1 + \frac{\Gamma}{12\Gamma_0} \cos \alpha_{fr}\right)}, \tag{36}$$

with Γ_0 the no-wind no-slope ROS, Γ the ROS and α_{fr} the flame tilt angle.

When R_{fr} does not play a significant role, that is, when the flame axis is normal to the ground or tilted toward the already burned vegetation, Eqs. (31) and (33) yield to the no-wind-no-slope ROS formulation:

$$\Gamma_0 = \frac{\varepsilon_{fr} \sigma_{sb} T_{fr}^4 \delta_v}{2\dot{m}_v'' \left(c_p \left(T_{ign} - T_{air}\right) + m_{H2O}'' \Delta h_m\right)}. \tag{37}$$

When $\alpha_{fr} > 0$, the flame is tilted toward the unburnt vegetation; the heat flux impinging of the fuel is stronger, and therefore the ROS is also larger. Combining Eqs. (31) and (33) in this case leads to the following ROS formulation:

$$\Gamma = \frac{1}{2} \left(R_a + \sqrt{Ra^2 + \frac{4\Gamma_0 \left(12\Gamma_0\right)}{\cos \alpha_{fr}}} \right), \tag{38}$$

with R_a and A_{fr} satisfying:

$$R_a = \Gamma_0 \left\{ 1 - \frac{12}{\cos \alpha_{fr}} + \frac{12 \nu_v \chi_{rad,0} \Delta h_c}{4 c_p \left(T_{ign} - T_{air}\right) + m_{H2O}'' \Delta h_m} A_{fr} \right\}, \tag{39}$$

$$A_{fr} = \frac{1 + \sin \alpha_{fr} - \cos \alpha_{fr})}{\cos \alpha_{fr}}. \tag{40}$$

2.3 FireFly, a data-driven wildfire spread model

Jointly developed by CERFACS and the UMD (University of Maryland), FireFly[1] is a software that represents wildfires as propagating fronts. There are different versions:

- a deterministic version (to simulate a free run);
- an ensemble-based version (to simulate an ensemble of free runs based on perturbations in the input parameters of the ROS model);
- a data-driven version based on the ensemble Kalman filter and sequentially assimilating observed fire front location.

These different versions are based on the same Fortran90 package, which is interfaced with the OpenPALM dynamic coupling software[2] (Lagarde et al., 2001).

A schematic of the FireFly simulator is presented in Fig. 6. This system requires six main components presented in the following:

- inputs;
- ROS model;
- front-tracking solver;
- isocontour identification;
- computation of the distance between simulated and observed fire fronts;
- data assimilation algorithm.

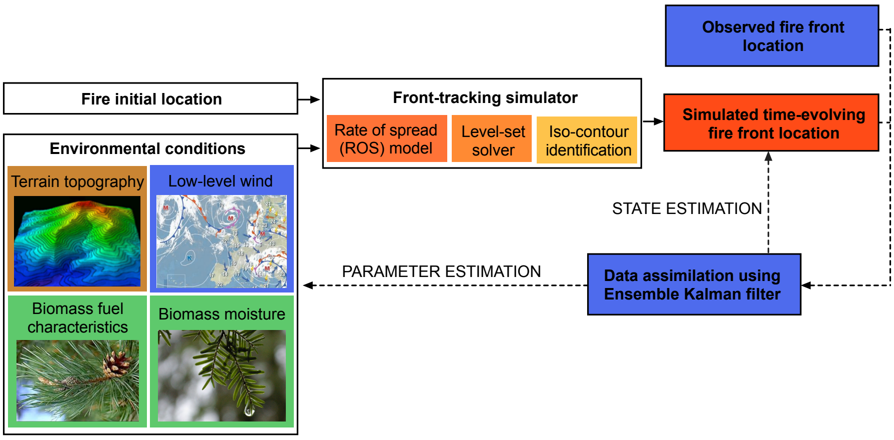

Figure 6: FireFly flowchart. Credits: Rochoux (2014a).

2.3.1 ROS model

In FireFly the 1-D ROS formulation due to Rothermel (1972) was generalized for a wind-aided fire propagation over a complex terrain topography. The new formulation reads:

$$\Gamma = \frac{\Gamma_0 \max\left(1, 1 + \cos\left[\theta_{fr} - (\theta_w + \Pi)\right]\Phi_w^* + \cos[\theta_{fr} - (\theta_a + \Pi)]\Phi_{sl}^*\right)}{\sqrt{1 + \tan^2(\theta_{sl})\cos^2\left(\theta_a - \theta_{fr}\right)}}, \quad (41)$$

[1] http://sophiericci.neowordpress.fr/
[2] http://www.cerfacs.fr/globc/PALM_WEB/

where Γ_0 is the no-wind-no-slope ROS, Φ_w^* the wind correction coefficient, Φ_{sl}^* the slope correction coefficient, θ_{fr} the normal direction to the fire front on the horizontal plane, θ_w the wind direction angle representing the direction from which the wind blows on the horizontal plane, θ_a the slope aspect angle representing the downhill direction on the horizontal plane, and θ_{sl} the slope direction angle. The slope aspect angle and the wind direction angle as well as the wind blowing direction and the uphill direction are defined in Fig. 7. These angles are defined starting from the North direction (0°), in the clockwise direction.

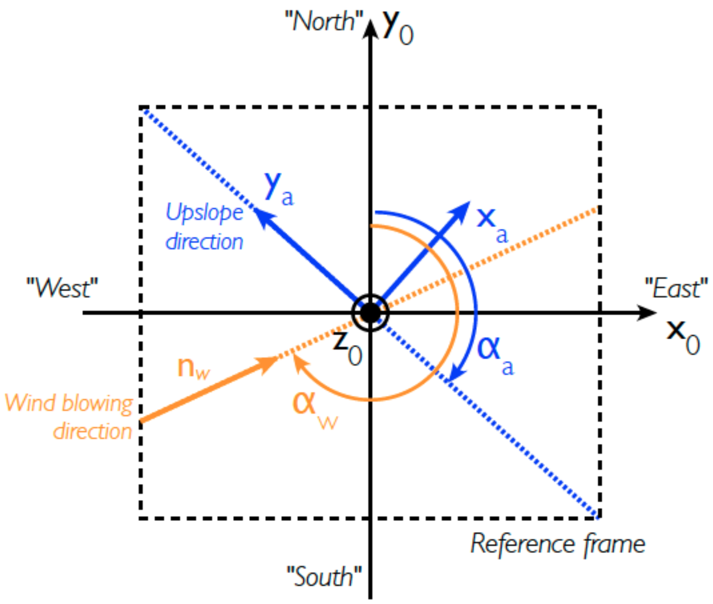

Figure 7: Representation of the topographical aspect angle θ_a (α_a in the figure) and the wind angle θ_w (α_w in the figure) on the horizontal reference frame (x_0, y_0, z_0). Credit: Rochoux (2014a).

The division by $\sqrt{1 + \tan^2(\theta_{sl}) \cos^2(\theta_a - \theta_{fr})}$ corresponds to the projection of the 1-D ROS on the two-dimensional horizontal plane, while the terms $\cos\left[\theta_{fr} - (\theta_w + \Pi)\right]$ and $\cos\left[\theta_{fr} - (\theta_a + \Pi)\right]$ correspond to the projection of the wind and slope correction coefficients on this same plane.

See Section 2.1 for more details on the formulation of the no-wind-no-slope ROS Γ_0 and on the correction coefficients Φ_{sl}^* and Φ_w^*.

2.3.2 Front tracking solver

A two-dimensional progress variable field noted $c = c(x, y, t)$ is introduced as a flame marker on the horizontal plane: $c = 0$ in the unburnt vegetation, $c = 1$ in the burnt vegetation, and the flame is the region where c takes values between 0 and 1. The flame front is thin and is conveniently identified as the isocontour $c_{fr} = 0.5$. The progress variable c is calculated as the solution of the following propagation equation:

$$\frac{\partial c}{\partial t} = -\gamma . \nabla c = \Gamma \, |\nabla c|, \tag{42}$$

with $\Gamma = \gamma.\mathbf{n}_{fr}$ the propagating speed along the normal direction to the front $\mathbf{n}_{fr}$ defined consistently with θ_{fr} as follows:

$$\mathbf{n}_{fr} = -\nabla c / |\nabla c|. \tag{43}$$

Since Eulerian approaches naturally handle complex and dynamic topology of fire

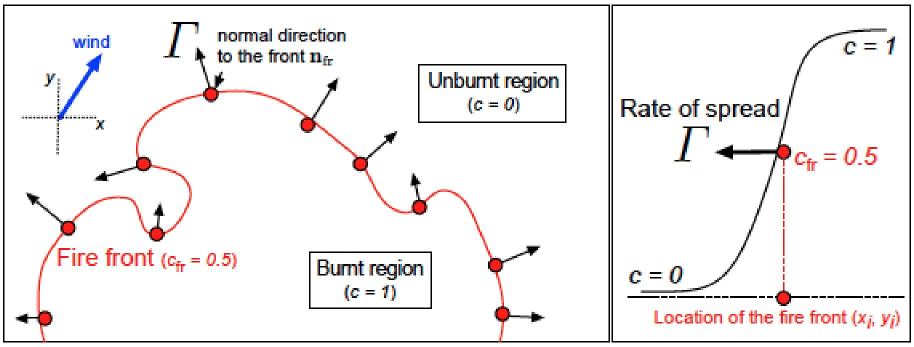

Figure 8: Schematic of the front-tracking solver. Left: the fire front is the contour line $c_{fr} = 0.5$; Γ measures the local ROS of the fire along the normal direction to the front $\mathbf{n}_{fr}$. Right: Profile of the spatial variations of c across the fire front, $(x_i; y_i)$ representing the location of the ith front marker. Credits: FireFly technical reference.

fronts such as collisions and merging, FireFly adopts a front-tracking approach based on a level-set approach inspired from Rehm and McDermott (2009). The basic steps of the numerical scheme are as follows:

(1) Computation of the node-centered gradient using a centered finite difference scheme:

$$\left(\frac{\partial c}{\partial x}\right)^t_{i,j} = \frac{c^t_{i+1,j} - c^t_{i-1,j}}{2\Delta x}, \tag{44}$$

$$\left(\frac{\partial c}{\partial y}\right)^t_{i,j} = \frac{c^t_{i,j+1} - c^t_{i,j-1}}{2\Delta y}, \tag{45}$$

with Δx a uniform mesh stepsize along the x-direction and Δy its counterpart along the y-direction, i and j corresponding to the index of the grid node, and t to the time step index.

(2) Computation of the unit normal vector $(\mathbf{n}_{fr})^t_{i,j}$, i and j corresponding to the normal direction to the fire front at the grid node indexed by the pair (i, j) using Eq. (43), with:

$$|\nabla c| = \sqrt{\frac{\partial c}{\partial x}^2 + \frac{\partial c}{\partial y}^2}\,. \tag{46}$$

▷ Computation of the flame velocity vector $\gamma^t_{i,j}$ using:

$$\gamma_x = \Gamma.\mathbf{n}_{fr,x}, \tag{47}$$

$$\gamma_y = \Gamma.\mathbf{n}_{fr,y}, \tag{48}$$

where x and y are the components of the flame velocity vector along the x- and y-directions.

(3) Determination of the monotonicity preserving scalar gradient r_{ct} at time t, for the propagating equation with a Superbee slope limiter (due to Toro 1999 and Rehm and McDermott 2009) in order to avoid high values of gradients near any zone of shock or discontinuity.

(4) Time-integration of the alternative formulation of the propagating equation, Eq. (49), from time t to time $(t+1)$, using a second-order Runge-Kutta scheme defined as a linear combination of two forward Euler steps:

$$\frac{\partial c}{\partial t}(x, y, t) + \gamma_x \frac{\partial c}{\partial x} + \gamma_y \frac{\partial c}{\partial y} = 0. \tag{49}$$

2.3.3 Isocontour identification

Once the spatio-temporal variations of the progress variable c are known, the location of the fire front is extracted using a simple isocontour algorithm such that, formally, the outputs of the front-tracking simulator are $[(x_i;\ y_i);\ 1{:}N_{fr}]$. $(x_i;\ y_i)$ represents the two-dimensional coordinates of the N_{fr} front markers obtained at time t (the index i indicating the marker), the fire front being identified as the isocontour $c_{fr} = 0.5$. The FireFly-simulated fire front (SFF) described by the N_{fr} markers corresponds to a fine-grained discretization of the fire front.

2.3.4 Comparison to the observed fire front

The current version of FireFly assumes that airborne and/or spaceborne observations of the fire front location are available at frequent time intervals but possibly provide an inaccurate and incomplete description of the fire front due to the opacity of the fire-induced thermal plume or due to a limited monitoring. See Rochoux (2014a) for a comprehensive review of remote wildfire spread monitoring.

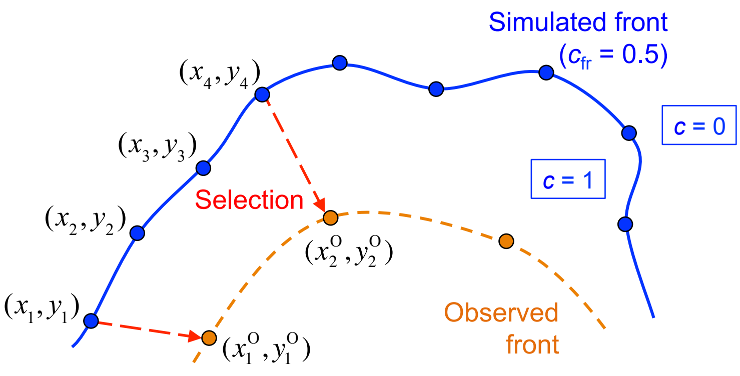

Figure 9: Schematic of the mapping process in FireFly. The isocontour algorithm selects one SFF marker out of every r SFF markers and associates it to the corresponding OFF marker. Then the distance between SFF and OFF is computed for every pair of markers. Here $r = N_{fr}/N_{fr}^o = 4$. Credit: Rochoux (2014a)

In FireFly, the observed fire front (OFF) is represented as a segmented line using a pre-defined number of equally-spaced markers (i.e., the N_{fr}^o observation markers). The observation vector noted $\mathbf{y}_t^o$ contains the two-dimensional coordinates $(x_i^o;\ y_i^o)$ of the front markers at the observation time (i corresponding to the index of a particular marker in the observation vector, with i varying between 1 and N_{fr}^o). These coordinates are assumed to have independent Gaussian-like random errors ε_o with zero mean and with standard deviation (STD) σ_o. The size of the observation vector $\mathbf{y}_t^o$ is $2N_{fr}^o$.

Since observations of the fire front location are likely to be provided with a much coarser resolution than FireFly's simulation and since they may cover only a fraction of the fire front perimeter, N^o_{fr} is much lower than N_{fr}. Thus, the observation operator consists in determining the equivalent of the N^o_{fr} observed markers onto the simulated isocontour $c_{fr} = 0.5$. This operation is performed through an operator $\mathcal{H}$, described in this case as an operator that selects 1 out of every r SFF markers, with $N^o_{fr} = N_{fr}/r$ and r an integer taking values (much) larger than 1. The selected SFF markers are associated with the nearest OFF marker, and the distance between the pair of markers is computed in order to define the innovation vector (i.e., the difference between the observations and their model counterparts in a data assimilation methodology). Preliminary tests have indeed shown that this simple treatment shown in Fig. 9 provides reasonable results.

However, different projection schemes are available and appear as a promising approach for properly capturing the topology of the fire front along with the heterogeneities of wildfire spread and thereby, for applying data assimilation to regional-scale wildfire spread. Further details are provided in Rochoux (2014a).

3 Tools and experimental settings

3.1 Technical implementation with OpenPALM

3.1.1 Generalities

OpenPALM is a dynamic code coupler developed in cooperation between CERFACS and ONERA (Office national d'études et de recherches aérospatiales) since 1996. OpenPALM software is a library of functionalities, used for applications from operational data assimilation to multi-physics modeling, climate change impact assessment or fluid/structure interactions. The OpenPALM coupler is used for two different purposes illustrated in Fig. 10: data parallelism and task parallelism. This work relies on the task parallelism aspect. OpenPALM is used to launch code units in a sequential manner, branch by branch or simultaneously. It is a convenient and efficient way to run these code units, sequentially or simultaneously, as well as to exchange data between them.

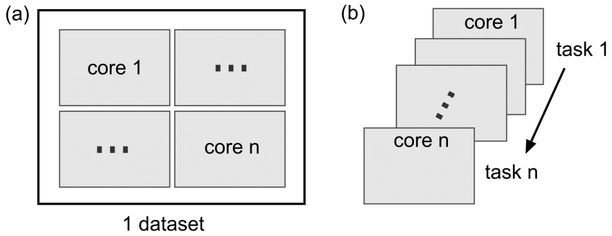

Figure 10: Different forms of parallelism. (a) Data parallelism. (b) Task parallelism. Credit: Rochoux (2014a).

3.1.2 OpenPALM components

OpenPALM is mainly made of three complementary components: the PALM library, the CWIPI library and the graphical interface PrePALM.

With regard to the PALM library, applications are split into elementary components that can exchange data through message passing interface (MPI) communication. The library is very efficient (dynamic launching of the coupled components, full independence of the components from the application algorithm, parallel data exchanges with redistribution and separation of the physics from the algebraic manipulations performed) and offers the option to merge into a single executable the coupled components that are started in a sequence.

The CWIPI (Coupling With Interpolation Parallel Interface) library provides a fully parallel communication layer for mesh-based coupling between different parallel solvers with MPI communications. The main feature of CWIPI involves construction of the communication graph between distributed geometric interfaces through geometrical localization (interpolation on non-coincident meshes, exchange of coupling fields for massively parallel applications, etc.).

PALM applications rely on a graphical user interface (GUI) called PrePALM (see Fig. 11). This interface initially defines the coupling (e.g., number of components, sequential and parallel sections) and makes an identity card for each coupled component. PrePALM is composed by branches, units, connections, etc. Code units are launched by branches through a branch code (logical operations such as if-loop or while-loop can also be performed in every branch, outside the code units). These units could be subroutines or a full solver; in any case, they are encapsulated as a sub-program in the main program generated and managed by OpenPALM. PrePALM produces the input file for the coupler executable and the source code for the wrappers of the coupled component that manage the set-up of the communication framework.

- In Fig. 11, there are two branches, three unit boxes and one communication line. Branches start together because they are on the StartOn mode, unit 1 and unit 2 are launched simultaneously but unit 2 waits for an input argument from unit 1. Unit 3 starts when unit 1 is finished, independently from the status of the unit 2.

- Figure 12 represents a simple unit box with two connections: a input pads (PALM_Put) and a output pads (PALM_Get). The unit box can be coded in several languages (Fortran, C, Python, Octave, etc.), but an identity card specific to OpenPALM needs to be implemented at the head of each code unit (this identity card specifies the dependence on modules and/or subroutines as well as the size of the variables to exchange for example).

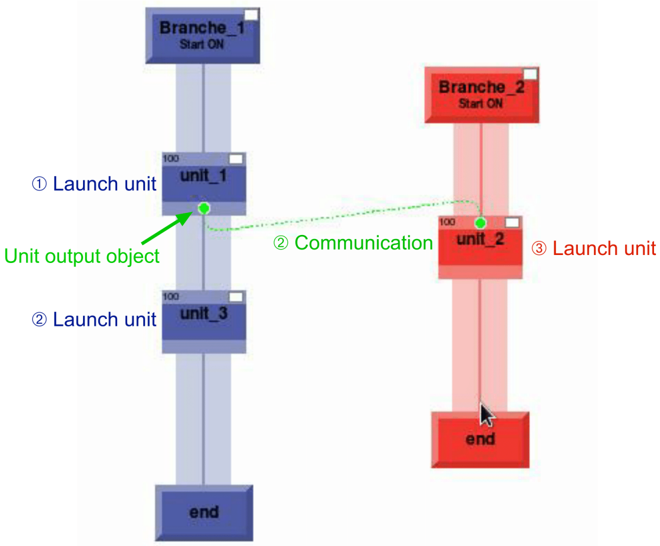

Figure 11: Example of a simple PrePALM interface with two branches, three units and one communication exchange between unit 1 and unit 2. Credit: Rochoux (2014a).

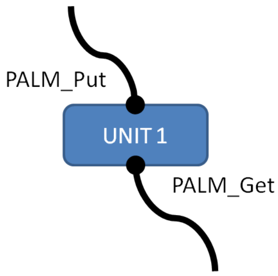

Figure 12: Example of unit box, requiring an input through the PALM_Put command and delivering an output variable to the OpenPALM environment through the PALM_Get command.

3.2 FireFly technical implementation

The FireFly prototype is made of three main components: a PrePALM interface, a make file whose goal is to generate a unique executable and a Fortran90 package made of subroutines called in different branches. The PALM driver manages the coordination of the different tasks and programs. Figure 3.2 presents the PrePALM interface for the deterministic version of FireFly. Using OpenPALM, a single executable is generated for the different units shown on the PrePALM interface. These units represent Fortran90 subroutines, the connection lines represent the exchange of data (input and output arguments of the code units) and each branch is devoted to a specific task inside the fire spread model.

3.2.1 Front-tracking simulator

i Input arguments

Input parameters are geographical conditions (latitude, longitude, altitude), meteorological conditions (wind speed and direction) and biomass fuel conditions (type and properties of biomass fuel species).

With regard to the model initial condition, the fire spread model requires a two-dimensional field c corresponding to the state of the burning zone. For synthetic cases, FireFly can be initialized using pre-defined initial fire configurations. For a real-case, the first available observation needs to be provided to the model as a binary field ($c = 0$ where the vegetation is unburnt and $c = 1$ where the vegetation is already burnt), which can be regarded as the model initial condition after detection.

ii Description of the units

As shown in Section 3.1, PrePALM is a graphical interface that shows the different links between the branches, the inputs, the outputs, etc. It presents the different units underlying the code. The PrePALM interface specific to FireFly (see Fig. 13) is made of five branches: topographic conditions, wind conditions, biomass fuel conditions, fire initial condition and fire model integration. On each branch, there are unit boxes which are related (by an identity card) to a Fortran main code. Each unit box can have several input arguments and/or outputs represented as nodes in Fig. 13 and these input/output arguments (of different types: integer, character, string, etc.) can be transferred between units through the communication lines.

The routine MAKE_TOPO is the first unit to be executed because the related branch (TOPOGRAPHY, yellow branch) is on the StartON mode. At the end of this subroutine, there are two output elements (green and pink circles corresponding to the aspect and slope angles), which are used by the RUN_FIREFLY_D unit (MODEL, red branch). Then, the WIND branch starts, producing the wind velocity field and running in-turn the BIOMASS_FUEL branch that provides the distribution and the properties of the biomass fuel models. The IC branch starts to generate the model initial condition. All these variables are provided to the RUN_FIREFLY_D unit as two-dimensional fields defined on the fire spread model grid; this unit runs the deterministic (D) version of FireFly, a single instance of the fire spread model.

3.2.2 Compilation

To run the deterministic version presented in Fig. 13, there is a three-step procedure to follow:
1) the generation of the PALM service files to translate the PrePALM scheme into a code source that can be read by the PALM library (CODE 1);

Figure 13: PrePALM interface specific to the deterministic version of FireFly. Credit: Rochoux (2014a).

2) the generation of a single code executable (palm_main) to be able to run the application (CODE 2);
3) the execution of the PALM executable palm_main (CODE 3).

```
CODE 1: $PREPALMMPDIR/prepalm_tclsh.tcl -no-make-include -c *.ppl
CODE 2: make
CODE 3: mpiexec -np 1 ./palm_main
```

3.2.3 Output arguments

As shows in Fig. 3.2, the RUN_FIREFLY_D unit has no output argument, output variables being indeed saved in external files through the routines (SAVE_FIELD, SAVE_SCALAR_TIME, SAVE_FRONT_XYZ, SAVE_FRONT_VAR and SAVE_FUEL). For each simulation, the routine fills in each folder (cvar, fi, front, ros and time) with simulations results at 100-s time intervals. The out directory contains the model diagnostics over time (time directory) as well as the time-evolving progress variable (cvar directory), the fireline intensity (fi directory), the front location (front directory) and the fireline rate of spread (ros directory).

3.2.4 Post-processing with Matlab

The output files from FireFly can be visualized using Matlab scripts located in the directory named POSTPROCESSING. The main MATLAB script (main_firefly_post.m) produces figures of the terrain topography, the biomass fuel distribution, the time-evolving location of the fire front (projected onto the horizontal plane or along the terrain topography), the progress variable field at regular time intervals, model diagnostics over time (in terms of mean front speed and mean front thickness along the fireline at a given time), the Rothermel-based rate of spread or fireline intensity distribution along the fireline at regular time intervals.

3.2.5 Simulation cases

Several examples of simulation cases (with or without wind) are presented below for illustration purposes.

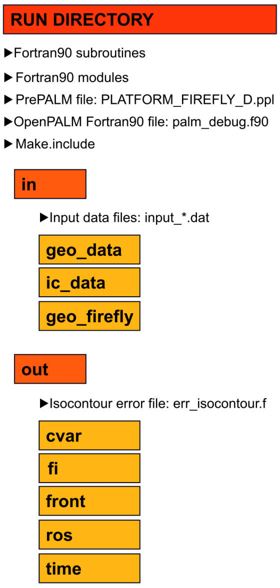

Figure 14: Architecture of the FireFly run directory. Credit: Rochoux (2014a).

i Case A

Case A shows the effects of the biomass fuel parameters (short grass), with no wind and flat terrain, a circular fire propagation and according to the Rothermel's ROS model. The initial fire corresponds to a circle of radius 5 m located in the center of the computational domain (200 m×200 m, described at 1-m resolution). In these conditions, the fire propagates in homogeneous conditions, i.e., at a constant and uniform rate of spread with $\Gamma = \Gamma_0 = 0.02$ m/s over a 1000-s time period (with a 0.5-s time step). Figure 15 shows the time-evolving location of the fire front at 100-s time intervals. Additionally, Fig. 16 presents the temporal variations of global fire spread variables: burnt area, fireline perimeter, front speed and thickness. The burnt area seems to increase exponentially with time, the fireline perimeter seems to increase linearly with time, the front speed remains constant and the front thickness is globally constant (a few mesh stepsizes). These results are consistent with a constant ROS and a perfectly circular propagation.

ii Case B

Case B shows the effects of wind parameters, with flat terrain, uniform biomass fuel, a circular fire propagation and according to the Rothermel's model. The initial fire is the same as case A (a circle of radius 5 m), but the wind conditions are different: the wind is spatially-distributed as shown in Fig. 17. Figure 18 presents the time-evolving location of the fire front at 100-s time intervals. The deformation of the fire front shape according to the wind direction angle is clearly visible (the fire propagation mainly occurs in the north-western direction). Figure 19 presents temporal variations of global fire spread variables: burnt area, fireline perimeter, front speed and thickness. The burnt area seems to increase exponentially with time, the fireline perimeter, seems to increase linearly with time, the front speed increases (ahile oscillating) and the numerical front thickness slightly increases over time. Graphics verified hypotheses of ROS and circular propagation.

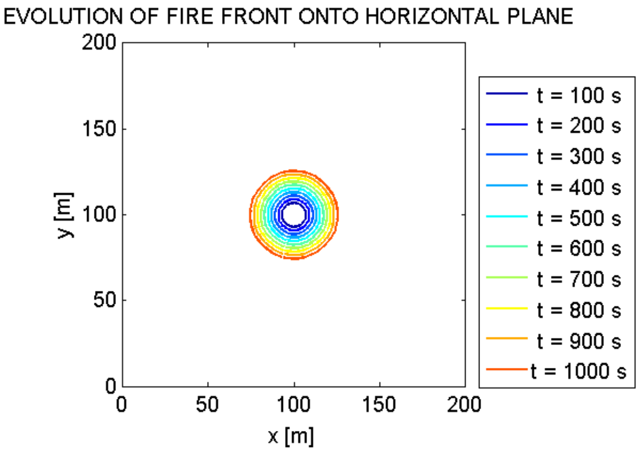

Figure 15: Case A with uniform biomass fuel, no wind, flat terrain; circular configuration; isotropic fire propagation. Time-evolving location of the fire front on the horizontal plane (x, y) over the 1000-s time period, at 100-s time intervals.

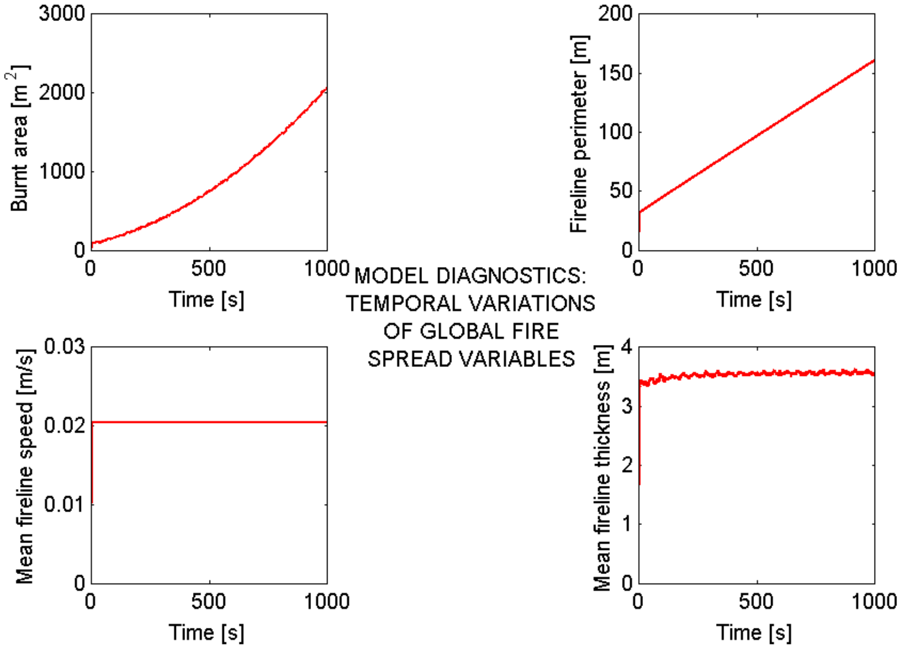

Figure 16: Model diagnostics over time for case A.

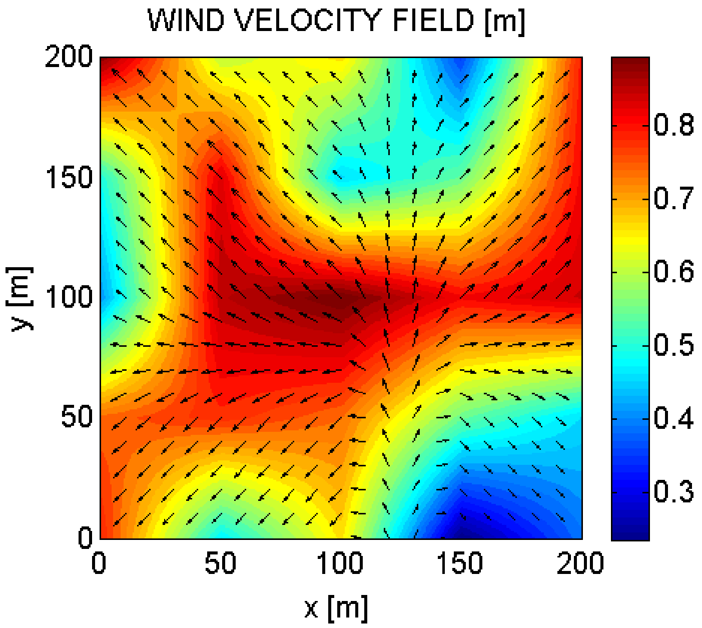

Figure 17: Case B with uniform biomass fuel, spatially-distributed wind, flat terrain; circular configuration; anisotropic fire propagation. Spatially-distributed wind field at the fire spread model resolution, the colorbar corresponds to the Wind speed [m/s].

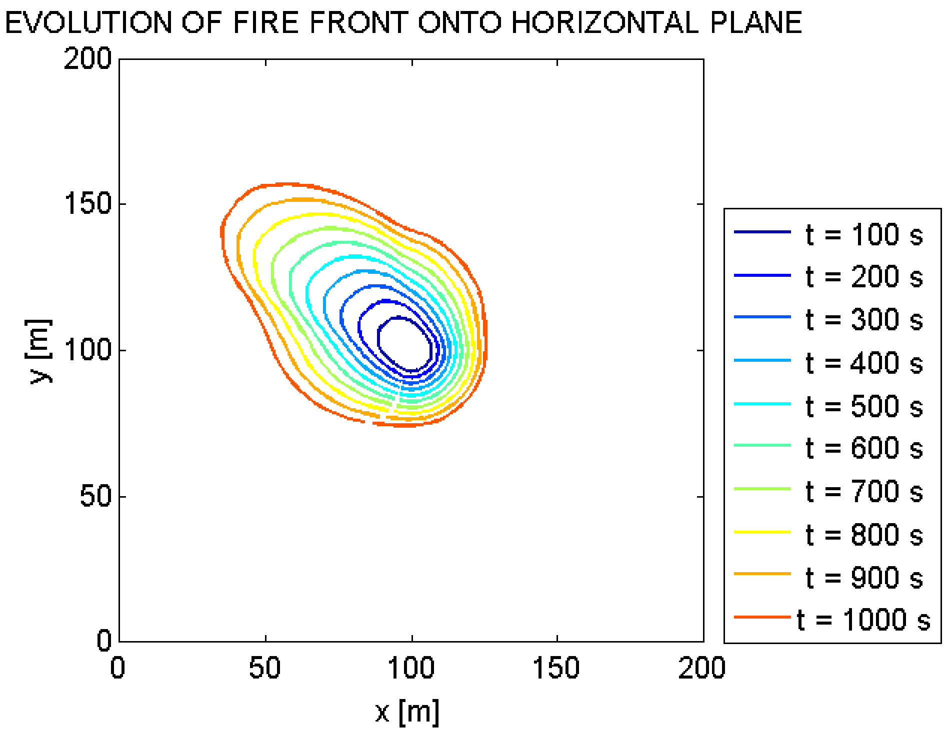

Figure 18: Case B with uniform biomass fuel, spatially-distributed wind, flat terrain; circular configuration; anisotropic fire propagation. Time-evolving location of the fire front on the horizontal plane (x, y) over the 1000-s time period, at 100-s time intervals.

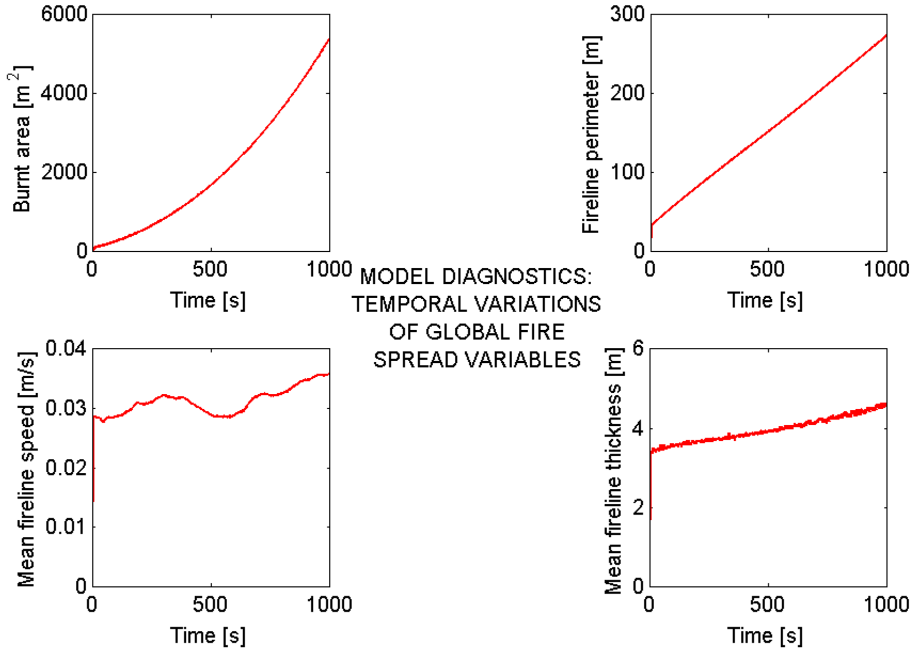

Figure 19: Model diagnostics over time for case B

3.3 The FireFlux experiment

3.3.1 Description of the controlled fire

Very few studies have been able to describe the atmospheric conditions within and during a wildland fire; even during prescribed burns, measurements are very limited. The aim of the FireFlux experiment (Clements, 2007) was then to collect data in order to better understand the fire-atmosphere interactions and to improve their modeling. In particular, the experiment was designed to document the flow and turbulence characteristics of both the fire–atmosphere interface and the plume within the fire perimeter and downwind of the burning area. This experiment was conducted in 2006 at the University of Houston Coastal Center (HCC). It still remains as one of the first and most comprehensive grass fire experiments to date, and serves as a standard for testing coupled fire–atmosphere modeling systems (Kochanski et al., 2013; Filippi et al., 2013).

HCC is located in Texas, approximately 45 km southeast of the Houston metropolitan area. HCC has a number of small-to medium-sized prairies that are categorized as Texas Gulf Coast tall-grass prairies consisting of a mixture of native grasses. The experimental prairie is 0.63 km^2 in size and consists of 90 % native species. In the morning of the burn (0900 CST-Central Standard Time) the temperature was 14.5 °C and the air humidity was 80 %. At the time of the burn, there were a temperature of 17.7 °C and a relative humidity of 63 %. The prairie was burnt the previous year for the pilot study. Figure 20 gives an overview of the experimental field along with the available measurement devices. Safety corridors were created all around the burn field. The fuel loading was estimated to be 1.08 kg/m^2.

3.3.2 Experimental data

As shown in Fig. 20, the meteorological instrumentation used during the experiment included:

- two instrumented towers: one is the main tower (43 m) located 100 m from the northern edge of the prairie; the second (10 m) is located 300 m South from the main tower (those towers were used to characterize the turbulent nature of the atmosphere);
- two sodars located on the East and West sides of the burn unit to capture the vertical wind structure;
- a tethered balloon system immediately downwind of the burn unit to describe the vertical structure of temperature, humidity, and wind in the fire plume;
- a weather station located approximately 100 m from the northern edge of the prairie to capture undisturbed ambient conditions immediately upwind of the burn unit.

Preliminary results indicated that fire-induced flows are very complex and that large upward vertical motion about 10 m/s can be associated with small grass fires, while downward vertical motion occurs behind the fireline. Measurements from the southern tower showed interesting features in terms of fire-induced circulations ahead of the fire front. Figure 21 shows a time series of 1-s-averaged 2-m wind and temperature obtained from the sonic anemometer and fine-wire thermocouples located on the little tower. At 1246:00 CST, 2-m-level winds shifted from northeasterly to easterly, and then at 1247:15 CST the winds became calm and shifted to southerly, indicating inflow into the approaching fire front. Soon after (1248:15 CST), the winds became

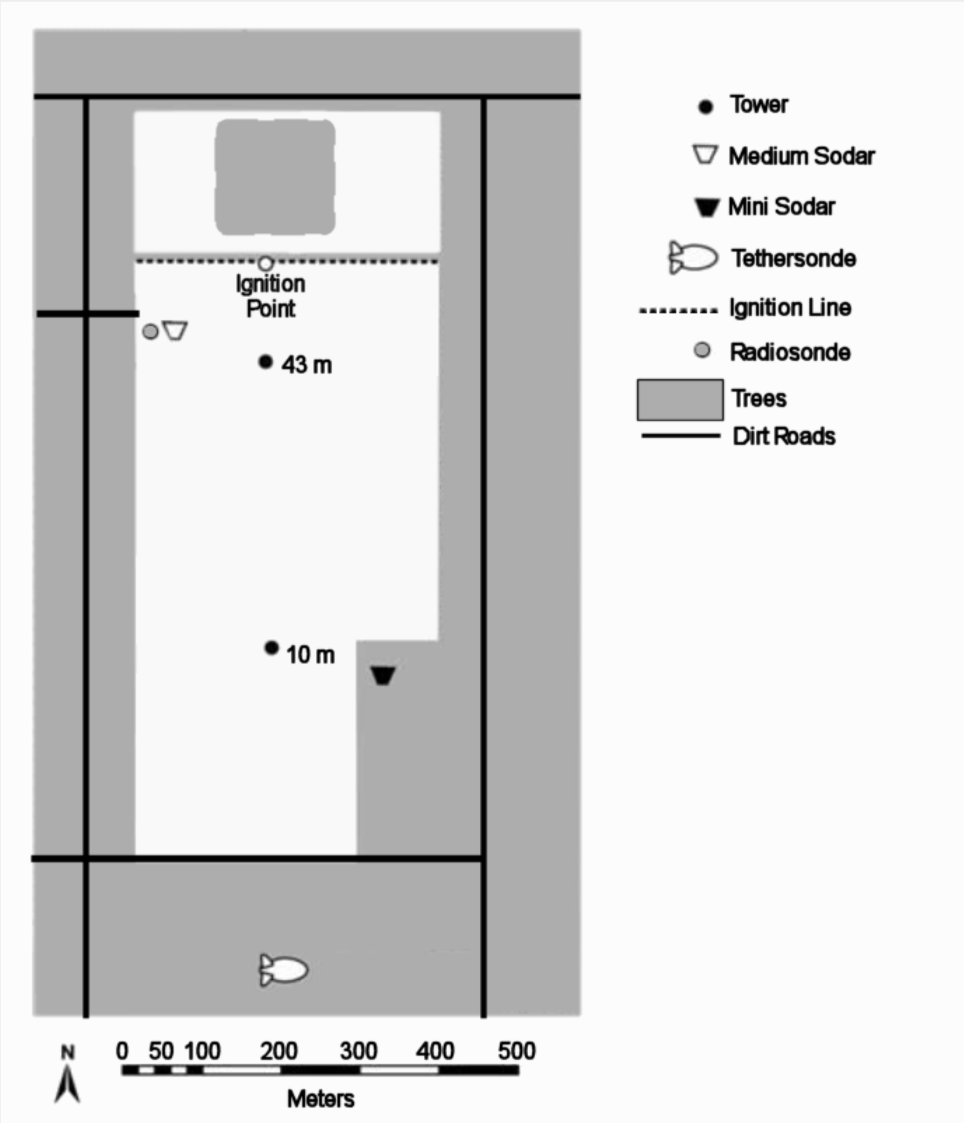

Figure 20: Map of the HCC experimental prairie and layout of instrumentation. Credits: Kochanski et al. (2013).

easterly and increased in magnitude to over 10 m/s. At 1250:10 CST the winds became calm again as vertical motion was very strong. Instantaneous upward vertical velocities were ≈ 7 m/s and downward velocities were over 4 m/s. This motion is associated with the horizontal vortex that occurred immediately in front of the fire front as observed at the main tower. Just after the vortex passed the tower, the fire front passed as indicated by the dramatic increase in temperature (up to 180 °C). At 1250:30 CST, winds immediately switched to a steady northerly flow, while downward motion occurred for the next 1.5 minutes. This period is associated with the downdrafts that occur behind the fire front and with horizontal winds that cross the fire line.

3.3.3 Fire–atmosphere coupled simulations

As shown in Fig. 22, fire-atmosphere interactions are complex and hard to model, since they involve multiple processes at the surface and in the atmosphere.

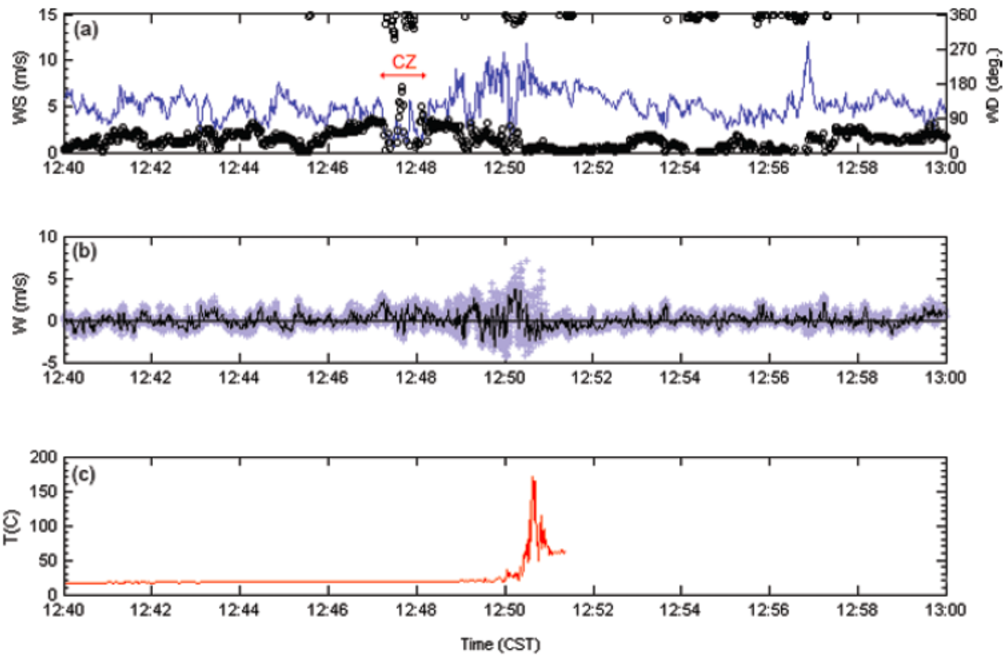

Figure 21: Time series of 1-s-averaged data from the 2-m sonic anemometer on the southern tower. (a) Horizontal wind conditions: the wind speed is indicated by the blue line, and the wind direction by the black circles. CZ indicates the convergence zone. (b) Vertical velocity (w), where blue crosses correspond to the instantaneous 20-Hz tilt-corrected values and the solid black line corresponds to the 1-s-averaged data. (c) Fine-wire thermocouples temperature (T). Credit: Clements (2007).

The FireFlux experiment was used to validate the coupled fire-atmosphere simulator integrating the meso-scale solver MésoNH and the fire spread model ForeFire developed at SPS (Filippi et al., 2009, 2013). The ROS model mainly used in ForeFire is the Balbi's model. Méso-NH is an anelastic non-hydrostatic mesoscale model, intended to be applied to all scales ranging from large (1000 m) to small scales (10 m). To validate this coupled fire-atmosphere simulator, three different simulations have been performed: first, non-coupled simulations with the stand-alone fire spread model ForeFire; then, coupled simulations at low resolution (25 m); and finally, coupled simulations at high resolution (10 m). Figure 23 shows the contours of the fireline progression for the three simulations at the observation times $t = 200$ s and $t = 460$ s. One can see that the main direction of propagation is different between the coupled and uncoupled simulations, this direction being indeed in much better agreement in coupled simulations at the short tower, even for the coarser 25-m case. Filippi et al. (2013) demonstrated that while the simulations did not reproduce high frequency perturbations, the atmospheric model captures well atmospheric perturbations induced by combustion at the ground level (in terms of behavior and amplitude).

Since the FireFlux experiment focused on the atmospheric properties, the location of the fire front was not monitored with a high temporal and spatial resolutions during the controlled burning. The arrival time of the fire front was only measured at the location of the two instrumented towers shown in Fig. 20. In this work, the results obtained with FireFly (with either the Rothermel's or the Balbi's ROS model) are compared to the MésoNH–ForeFire coupled simulations that were validated against observations (mainly related to atmospheric properties). Due to a lack of real observations, the comparison between the ROS formulations is therefore based on a simulator that integrates more physical processes and that was found to be more accurate than a stand-alone fire spread model.

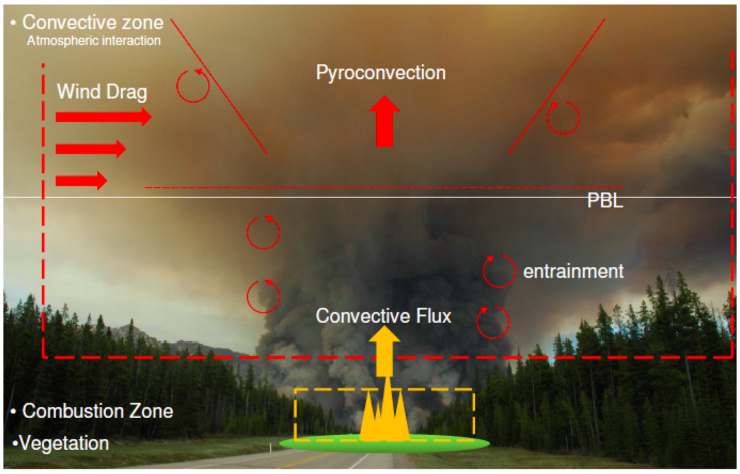

Figure 22: Schematic of fire–atmosphere interactions (PBL standing for planetary boundary layer). Credit: Martin Wooster (private communication).

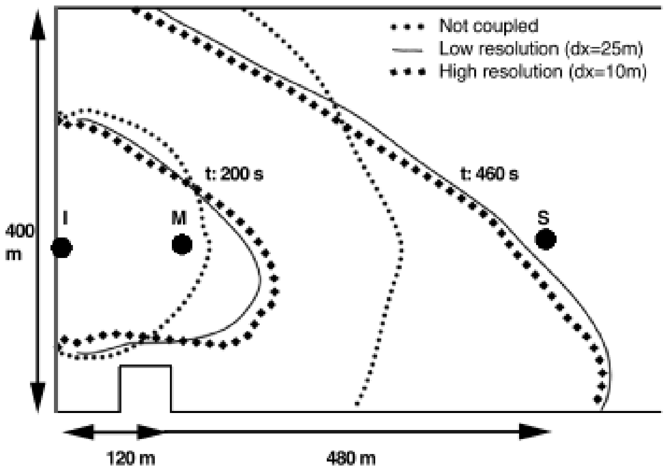

Figure 23: Bird's eye view of the FireFlux experimental setup: I stands for Ignition, M for Main tower and S for Short tower. Lines are isochrones at the time at which the experimental fire hit the towers. Credits: Filippi et al. (2013).

4 Comparison between Balbi's and Rothermel's ROS formulations

4.1 Sensitivity study with a simplified model

4.1.1 Sensitivity study

The aim of the present sensitivity study is to identify the most sensitive input parameters in both Rothermel's and Balbi's models, in order to check to which parameters the models are the most sensitive and which parameters should then be corrected through the FireFly data assimilation process. The EnKF algorithm is able to handle (at least partially) nonlinearities (unlike the standard Kalman filter). Still, it is important to identify to which parameters these nonlinearities are associated and how nonlinear is the interaction between a given input and the model output. Indeed, more members are usually required in the ensemble when this interaction is more nonlinear (the error statistics are more difficult to characterize).

Prior to the project, a 0-D Rothermel ROS function as well as a 0-D Balbi ROS function already existed (implemented in Matlab and referred to as *toy model* in the following). A Matlab code to study the sensitivity of Rothermel's ROS to the input parameters was also available. The first step of this project consists in extending this Matlab code to also perform the sensitivity analysis on Balbi's formulation, with an adaptation of the code to the new input parameters of Balbi's model (see Paragraph 4.1.2). Furthermore, two other code units were implemented in order to study the wind speed influence (see Paragraph 4.1.3). An exemple of this codes is available in the Appendix E.

The values of the input parameters used for this 0-D sensitivity study correspond to those of the FireFlux controlled fire experiment (see Section 3.3). An ensemble of 20 members is created, equally spread in an interval centered on the FireFlux reference value and with values varying from −50 % to +50 % of this reference value. The list of the input parameters under consideration and their range of variations are available in Table 2. Both Balbi's and Rothermel's ROS formulations are solved for each set of input parameters.

Figure 24 presents the variation of the no-wind no-slope ROS Γ_0 with respect to the fuel layer thickness δ_v varying between 0.75 and 2.25 m; the left panel corresponds to the Rothermel's ROS, while the right panel corresponds to the Balbi's ROS. It is found that both Balbi's and Rothermel's ROS models depend linearly on the fuel layer thickness, consistently with the corresponding analytical formulation: refer to Eqs. (4–(5)–(10)–(11) for Rothermel's model and to Eq. (39) for Balbi's model. However, the fuel layer thickness has a stronger influence on Γ_0 in Balbi's model, with values twice larger than those obtained in Rothermel's model.

Figure 25 presents the sensitivity of Γ_0 to the fuel surface loading. The left panel shows a nonlinear dependence of the Rothermel's ROS. This can be explained by the expression of the fuel packing ratio β_v (see Eqs. 9–10) and its nonlinear dependence on the optimum reaction velocity (see Eq. 6). In contrast, on the right panel, it is found that Balbi's ROS nonlinearly depends on the fuel surface loading and decreases when the latter increases. This is consistent with Eq. (39), because Γ_0 is inversely proportional to m_v''. Thus, the fuel surface loading has opposite effects on Rothermel's and Balbi's ROS values. As in both formulations, the fuel layer thickness is either part of the numerator or the denominator, the no-wind no-slope ROS can take significantly different values (from 0.03 to 0.3 m/s) depending on the choice of the ROS model.

With regards to the fuel moisture content, the left panel of Fig. 26 shows a nonlin-

Name	**Nominal value**	**Range of variation**
Fuel moisture content M_v [%]	9	[4.5; 13.5]
Fuel layer thickness δ_v [m]	1.5	[0.75; 2.25]
Fuel surface loading m''_v [kg/m^2]	1.08	[0.54; 1.62]
Fuel particle mass density ρ_p [kg/m^2]	400	[200; 600]
Fuel heat content Δh_c [J/kg]	15.43×10^6	[7.73×10^6; 23.2×10^6]
Fuel particle surface-to-volume ratio Σ_v [m^{-1}]	5000	[2500; 7500]
Flame temperature T [K]	1440	[720; 2166]
Flame emissivity ε_{fr}	5000	[2500; 7500]
Moisture evaporation enthalpy Δh_v [J/kg]	2.5×10^4	[1.25×10^4; 5×10^4]
Thermal capacity ε [J/K/kg]	2000	[1000; 3000]

Table 2: Input parameters under consideration in the 0-D sensitivity study: name, symbol, nominal value and range of variation.

ear dependence of the Rothermel's ROS Γ_0. It is most likely due to the moisture damping coefficient expression (see Eq. 12). On the right panel, the dependence of the Balbi's ROS Γ_0 is quasi linear and the moisture content has no significant impact on Γ_0. In both cases, the no-wind no-slope ROS is inversely proportional to the moisture content, but the range of variation is completely different: the moisture content has only a reduced effect on the Balbi's ROS, whereas it has a much more important effect on the Rothermel's ROS, especially for a moisture content between 0 and 5 %.

The sensitivity of the Rothermel's no-wind no-slope ROS to the fuel particle surface-to-volume ratio Σ_v is presented in Fig. 27; this dependence is linear. This is surprising, because, according to the theory, Γ_0 depends on Σ_v in a complex way (see Section 2.1): this dependence is not completely linear but tends to it. As for the Balbi's case, Balbi's no-wind no-slope ROS is not sensitive to Σ_v; this is confirmed by Eq. (39), where Σ_v is not present. Note however that Σ_v has a storng influence on the wind-aided slope-aided ROS Γ, through the expression of the radiation factor $\chi_{rad,0}$.

Figure 28 shows the dependence of Γ_0 to the fuel heat content Δh_c. In Rothermel's case, Γ_0 is proportional to the fuel heat content, consistently with Eqs. (4)–(5). In Balbi's formulation, there is no real dependence of Γ_0 on Δh_c. Note that it is still an important nput parameter to consider in the Balbi's ROS model due to its impact on the wind-aided slope-aided ROS Γ through the expression of the term R_a.

The sensitivity of the fuel particle density ρ_p on Γ_0 is presented in Fig. 28. There is almost no impact on both Rothermel's ROS and Balbi's ROS (see Eq. 30).

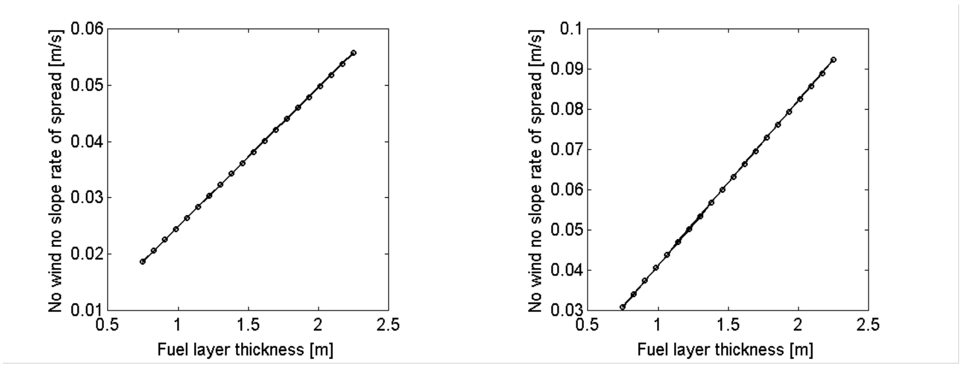

Figure 24: Variation of the no-wind no-slope ROS Γ_0 with respect to the fuel layer thickness δ_v. Left: according to Rothermel's ROS formulation. Right: according to Balbi's ROS formulation.

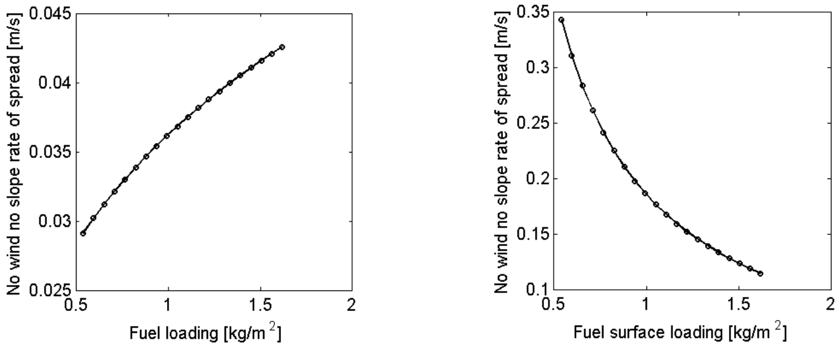

Figure 25: Variation of the no-wind no-slope ROS Γ_0 with respect to the fuel surface loading m''_v. Left: according to Rothermel's ROS formulation. Right: according to Balbi's ROS formulation.

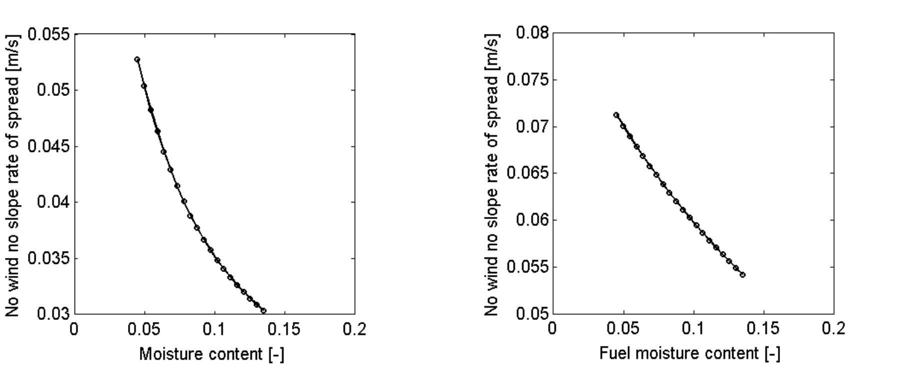

Figure 26: Variation of the no-wind no-slope ROS Γ_0 with respect to the fuel moisture content M_v. Left: according to Rothermel's ROS formulation. Right: according to Balbi's ROS formulation.

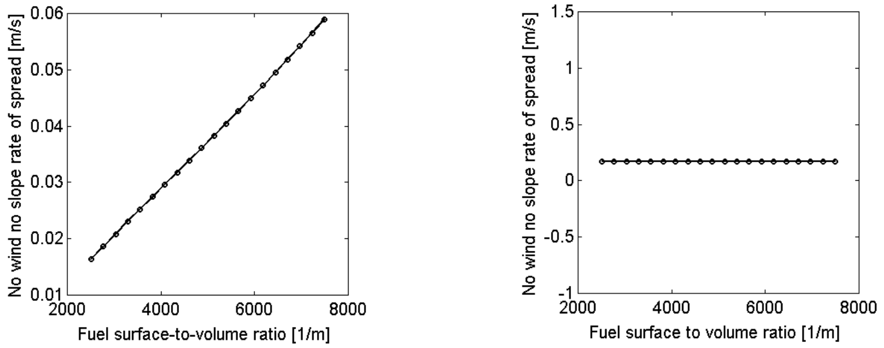

Figure 27: Variation of the no-wind no-slope ROS Γ_0 with respect to the fuel particle surface-to-volume ratio Σ_v. Left: according to Rothermel's ROS formulation. Right: according to Balbi's ROS formulation.

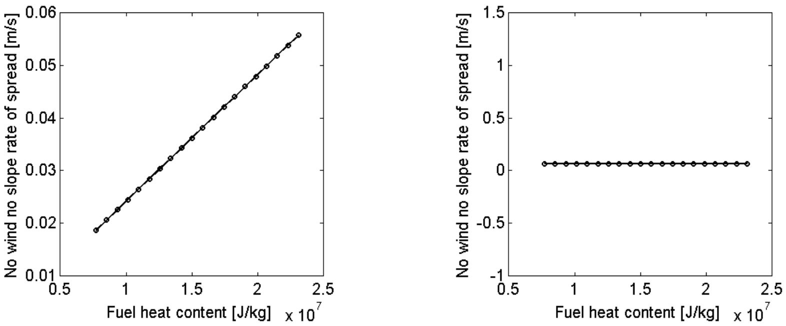

Figure 28: Variation of the no-wind no-slope ROS Γ_0 with respect to the fuel heat content Δh_c. Left: according to Rothermel's ROS formulation. Right: according to Balbi's ROS formulation.

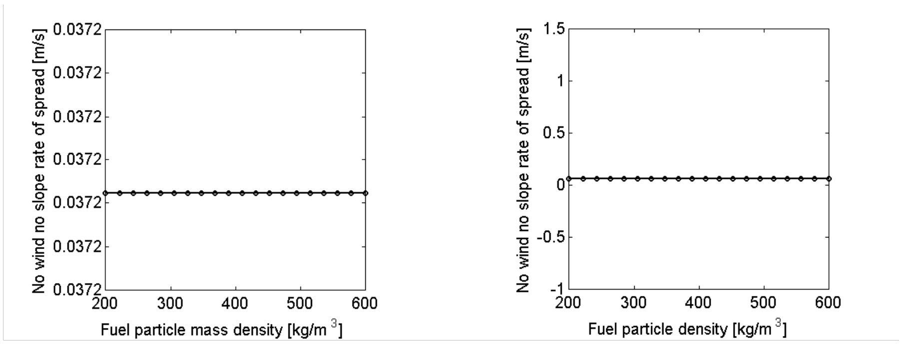

Figure 29: Variation of the no-wind no-slope ROS Γ_0 with respect to the fuel particle mass density ρ_p. Left: according to Rothermel's ROS formulation. Right: according to Balbi's ROS formulation.

The four plots presented in Fig. 30 show the sensitivity of the Balbi's no-wind no-slope ROS to parameters that are taken into account only in Balbi's formulation: the thermal capacity c_p, the flame emissivity ε_{fr}, the moisture evaporation enthalpy Δh_m and the flame temperature T_{fr}. The trends observed in these plots correspond to the analytical ROS formulation given in Eq. (39). First, Γ_0 is inversely proportional to the thermal capacity and to the moisture evaporation enthalpy (even though the interrelation between the ROS and the parameter is quasi-linear). Then, Γ_0 is proportional to the flame emissivity and nonlinearly depends on the flame temperature.

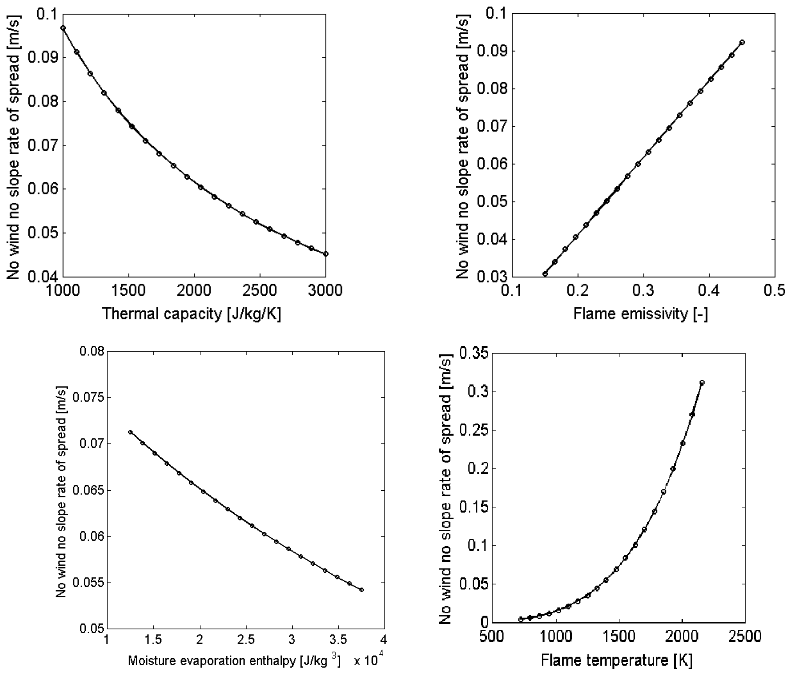

Figure 30: Variation of Balbi's no-wind no-slope ROS Γ_0 with respect to the thermal capacity c_p (top left panel), the flame emissivity ε_{fr} (top right panel), the moisture evaporation enthalpy Δh_m (bottom left panel) and the flame temperature T_{fr} (bottom right panel).

4.1.2 Parameter impact ranking on Balbi's no-wind no-slope formulation

The sensitivity study performed for Balbi's ROS model shows that each input parameter has a different influence on the ROS value. To be able to rank the input parameters according to their impact on the ROS value, Table 3 indicates the change in the ROS amplitude for each input parameter when perturbed by 50 % around the FireFlux reference value (the input parameters are sorted in decreasing order with respect to this ROS amplitude). It is found that the most important effect is due to the thermal capacity ε. In fact, when the fuel can store more heat, the fire front is slower; this is the main difference between Balbi's and Rothermel's ROS formulations (see Fig. 25). The second effect is due to the the flame temperature T. Then, there are the fuel surface loading m_v'', the flame emissivity ε_{fr}, the fuel layer thickness δ_v, the fuel moisture content M_v and the moisture evaporation enthalpy Δh_v. The impact of the fuel heat content Δh_c and the fuel particle surface-to-volume ratio Σ_v is not significant on the ROS value (with no-wind and no-slope conditions). This ranking is needed to define the data assimilation control vector in order to include parameters that have a strong impact on the ROS value.

Name and symbol	ROS amplitude [m/s]
Thermal capacity ε	-0.52
Flame temperature T	0.311
Fuel surface loading m''_v	-0.24
Flame emissivity ε_{fr}	0.061
Fuel layer thickness δ_v	0.061
Fuel moisture content M_v	-0.017
Moisture evaporation enthalpy Δh_v	-0.017
Fuel heat content Δh_c	0.000
Fuel particle mass density ρ_p	0.000
Fuel particle surface-to-volume ratio Σ_v	0.000

Table 3: Input parameters under consideration in the sensitivity study: name, symbol and ROS amplitude, sorted in decreasing order when considering the variation of the ROS when perturbing the input parameters by 50 % around the FireFlux reference case.

4.1.3 Impact of the wind

It is also important to study the impact of the wind u_w on the wind-aided slope-aided ROS Γ, in order to fully compare Rothermel's and Balbi's formulations. u_w corresponds to the mid-flame height wind velocity varying between 1.5 to 4.5 m/s. The resulting plots are an ensemble of plots with different colors (each color line represents a specific value of u_w, where the red line corresponds to a wind velocity of 1.5 m/s and the pink color corresponds to 4.5 m/s. For instance, Fig. 31 presents the variations of Γ with respect to the fuel layer thickness δ_v. It is shown that Γ can be multiplied by a factor 10 when the wind speed increases from 1.5 to 4.5 m in Balbi's formulation, the spread of the ROS values is much reduced for Rothermel's formulation.

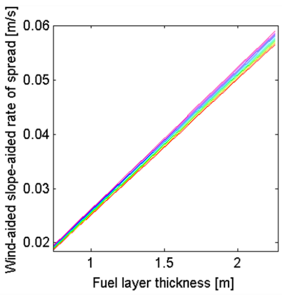

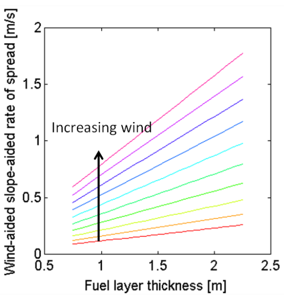

Figure 31: Variation of the wind-aided slope-aided ROS Γ with respect to the fuel layer thickness δ_v, with variation of the wind speed u_w. Left: with Rothermel's ROS formulation. Right: with Balbi's ROS formulation.

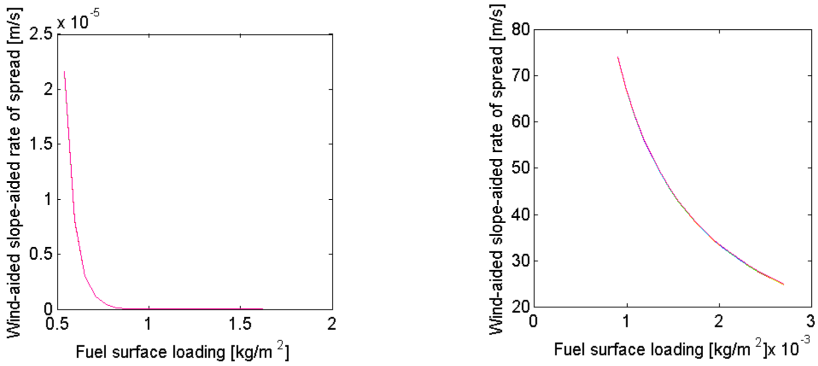

Figure 32: Variation of the wind-aided slope-aided ROS Γ with respect the fuel surface loading m''_v, with variation of the wind speed u_w. Left: with Rothermel's ROS formulation. Right: with Balbi's ROS formulation.

In Fig. 32, all the color lines match for both Rothermel's and Balbi's ROS models, implying that the impact of the fuel surface loading does not change when the wind speed increases. With regards to the fuel moisture content in Fig. 33, it is shown that the spread of the ROS values is smaller for Rothermel's model than for Balbi's model (the ROS can be multiplied by a factor of 10 if the wind blows at 4.5 m/s). Thus, the moisture content seems to be an important parameter to consider in a parameter estimation approach. Figure 34 presents the counterpart of Fig. 33 for the fuel particle surface-to-volume ratio Σ_v. The ROS values feature a much wider scatter for Σ_v in the case of Balbi's model than in the case of Rothermel's model. Note that in Rothermel's case, for values lower than 3000 m^{-1}, the sensitivity of the ROS to the wind speed u_w increases. Above this threshold value, the impact of the wind is not significant.

The four plots presented in Fig. 36 show the sensitivity of Balbi's ROS Γ to the same parameters as in Fig. 30, the thermal capacity c_p, the flame emissivity ε_{fr}, the moisture evaporation enthalpy Δh_m and the flame temperature T_{fr}. The spread of the ROS values for varying wind speed is wider for low values of the thermal capacity and of the moisture evaporation enthalpy. Moreover, the nonlinear dependence of the ROS to the thermal capacity increases with the wind velocity. Both the ROS dependence to the flame emissivity and the flame temperature is stronger when the wind velocity increases. The spread for varying wind speed is significantly reduced for low values of the flame temperature, while it nonlinearly increases for high values.

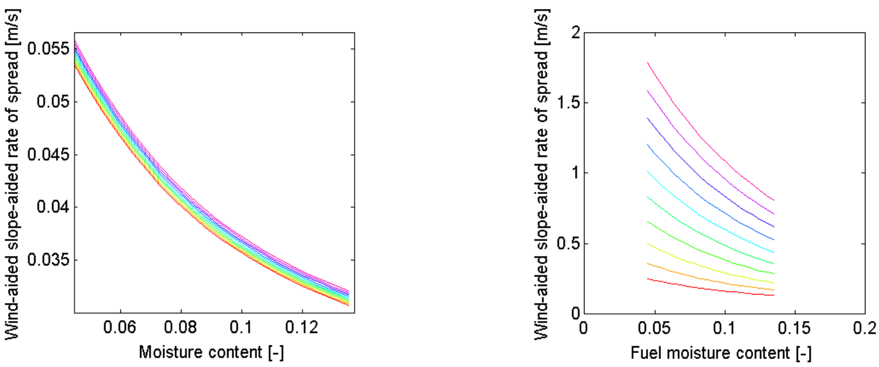

Figure 33: Variation of the wind-aided slope-aided ROS Γ with respect to the fuel moisture content M_v, with variation of the wind speed u_w. Left: with Rothermel's ROS formulation. Right: with Balbi's ROS formulation.

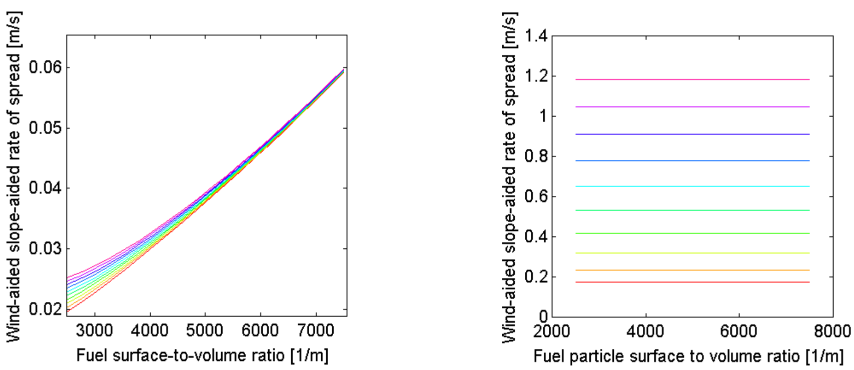

Figure 34: Variation of the wind-aided slope-aided ROS Γ with respect to the fuel particle surface-to-volume ratio Σ_v, with variation of the wind speed u_w. Left: with Rothermel's ROS formulation. Right: with Balbi's ROS formulation.

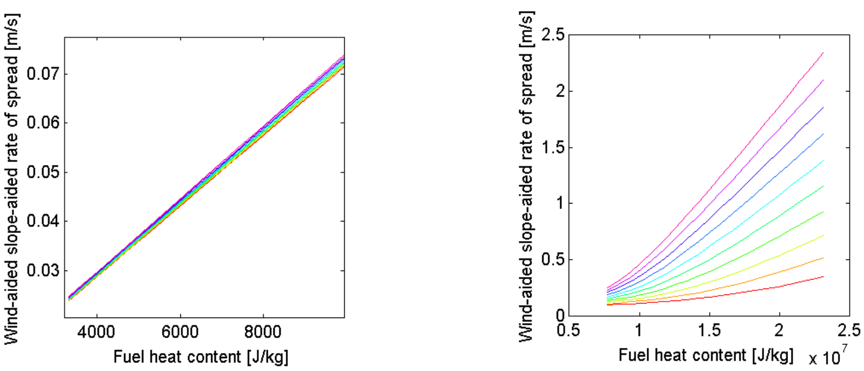

Figure 35: Variation of the wind-aided slope-aided ROS Γ with respect to the fuel heat content Δh_c, with variation of the wind speed u_w. Left: with Rothermel's ROS formulation. Right: with Balbi's ROS formulation.

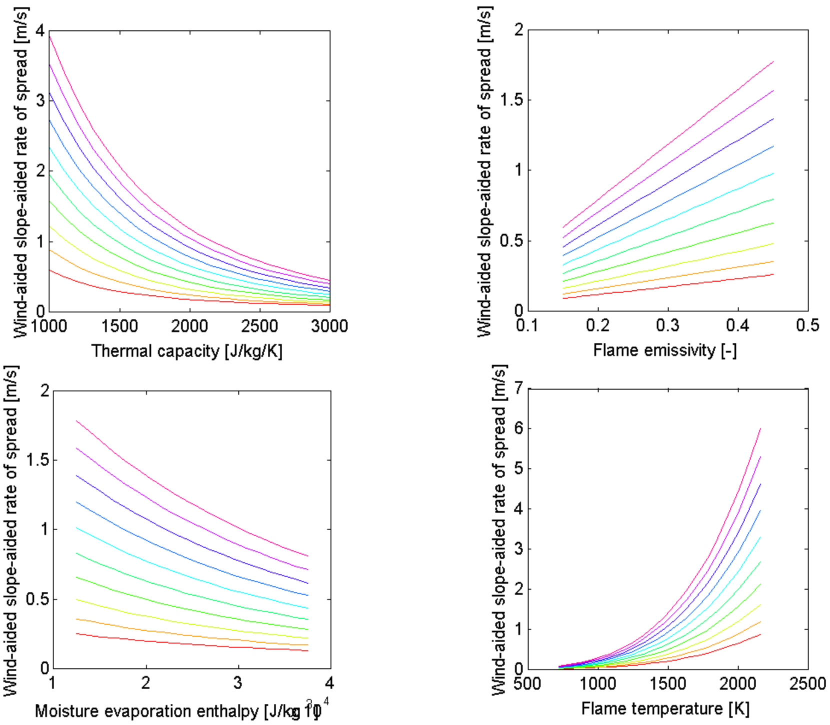

Figure 36: Variation of the Balbi's wind-aided slope-aided ROS Γ with respect to the thermal capacity c_p (top left panel), the flame emissivity ε_{fr} (top right panel), the moisture evaporation enthalpy Δh_m (bottom left panel) and the flame temperature T_{fr} (bottom right panel).

4.2 Balbi's ROS formulation implementation in FireFly

4.2.1 A test with Matlab

Before working on FireFly's code, the evaluation of the Balbi's ROS formulation (extended to 2-D configurations) in Matlab is useful to compare and verify the simulation results obtained in FireFly. The following reference test uses the FireFlux data presented in Table 4.

Name	Nominal value
Fuel moisture content M_v [%]	9
Fuel layer thickness δ_v [m]	1.5
Fuel surface loading m''_v [kg/m^2]	1.08
Fuel particle mass density ρ_p [kg/m^2]	400
Fuel heat content Δh_c [J/kg]	15.43×10^6
Fuel particle surface-to-volume ratio Σ_v [m^{-1}]	5000
Flame temperature T_{fr} [K]	1440
Flame emissivity ε_{fr}	0.3
Moisture evaporation enthalpy Δh_m [J/kg]	2.5×10^4
Thermal capacity ε [J/K/kg]	2000
Buoyancy velocity u_b [m/s]	2
Ignition temperature T_{ign} [K]	593
Air temperature T_{air} [K]	293
Ratio between incident radiant and ignition energy $A0 = \frac{\chi_{rad,0}\Delta h_c}{4c_p(T_{ign}-T_{air})}$	2.25

Table 4: Input parameters for the 2-D Balbi's ROS formulation used in the Matlab study; reference test.

The original Balbi's ROS model corresponds to a 0-D formulation. To extend it to a 2-D study, the solution is to use a 2-D wind field as input parameter. That is why, in the Matlab code, the 2-D Balbi's formulation is implemented with the wind determined as follows (see Appendix E):

$$u_w = u_w \max\left[0, \cos\left(\alpha_{fr} - (\alpha_w + \pi)\right)\right], \tag{50}$$

with α_{fr} [rad] the local normal direction to the front and α_w [rad] the wind direction from which the wind is blowing.

The ROS is simulated assuming an isotropic propagation starting from a circular front, meaning that the fire front remains circular over time in FireFly simulations (the local normal direction varying between 0 and 2π). The calculated ROS based on Balbi's model is presented in Fig. 37 on the left panel; the equivalent figure for Rothermel's ROS is provided on the right panel for comparison. The ROS in the upwind direction (i.e., the maximum ROS value) is higher with Balbi's model (2.07 m/s) than with Rothermel's model (1.38 m/s). Also, the ROS variation between the propagation in the opposite direction to the wind and the propagation in the wind direction is much sharper with Rothermel's formulation than with Balbi's formulation.

4.2.2 Implementation in FireFly

FireFly is implemented in Fortran (f90). Without the OpenPALM interface there are 12 Fortran files, including 5 main files (`MAKE_FUEL`, `MAKE_TOPO`, `MAKE_WIND`, `MAKE_IC`

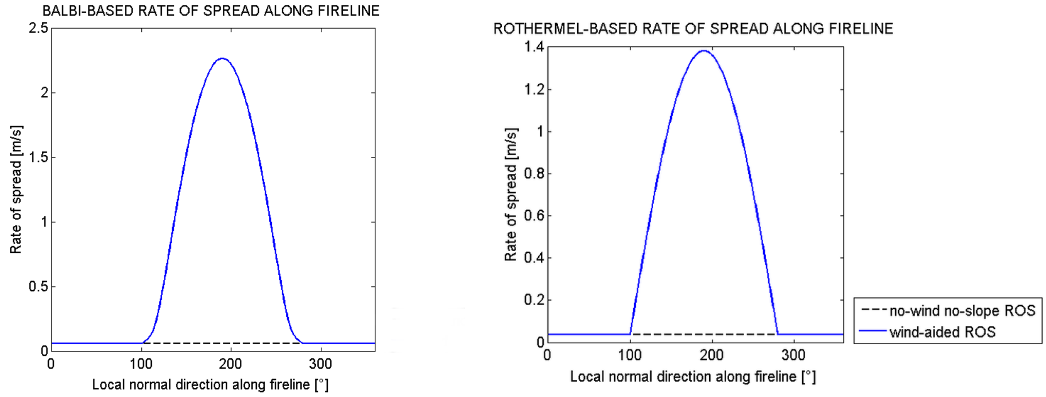

Figure 37: 2-D ROS value obtained with the Balbi's formulation (left) and the Rothermel's formulation (right) with respect to the local normal direction to the front α_{fr} in degrees; Matlab ROS simulations for the reference test. The blue solid line corresponds to the wind-aided ROS Γ; the horizontal black dashed line corresponds to the no-wind ROS Γ_0.

to generate the input data and the model initial condition at the model grid resolution on the one hand, `RUN_FIREFLY_D` with D standing for deterministic to run the fire spread model over a given time period on the other hand), 1 subroutine used for contour identification (`ISOCONTOUR_2DUNIF`), and 6 modules containing a list of subroutines related to one aspect of the fire spread model (`M_FIRE`, `M_RUN`, `M_FUEL`, `M_TOPO`, `M_WIND`, `M_GENERIC`), see the code flowchart presented in Appendix B (the principal module related to a main file and this main file are colored similarly).

To evaluate the ROS, only one module is used, namely `M_FIRE.f90`. In this module, there is already a subroutine `ROTHERMEL` called by the subroutine `FIRE_SOLVER`, in order to evaluate the Rothermel-based ROS value at each grid point of the computational domain (this operation being repeated at each time step of the model integration). To use another ROS formulation, it is convenient to implement a new subroutine `BALBI` (in parallel to `ROTHERMEL`), which allows to evaluate the Balbi-based ROS at each grid point (see the corresponding Fortran90 code in Appendix C). To implement this ROS model, the same approach as in the Matlab 2-D study is used.

To compare the results obtained with Rothermel's and Balbi's formulations, an isotropic test case with no wind, flat terrain and a circular fire front as initial condition is used first. Figure 38 shows the simulated fire front positions for both formulations. The main difference is the propagating speed, Balbi's ROS being higher than Rothermel's ROS by nearly a factor of 4. That is why the fire front propagates faster in Balbi's configuration than in Rothermel's configuration. Figure 39 presents the temporal variations of global fire spread variables. Consistently with the ROS results, the burnt area, the fireline perimeter and the mean fireline speed are higher with Balbi's formulation than with Rothermel's formulation. As for the mean fireline thickness, both formulations give approximately the same results (the numerical thickness corresponds to 3 to 4 mesh stepsizes).

A second test case, named B1b, with anisotropic fire spread conditions is used. It corresponds to a wind-aided fire propagation over a flat terrain and starting from a

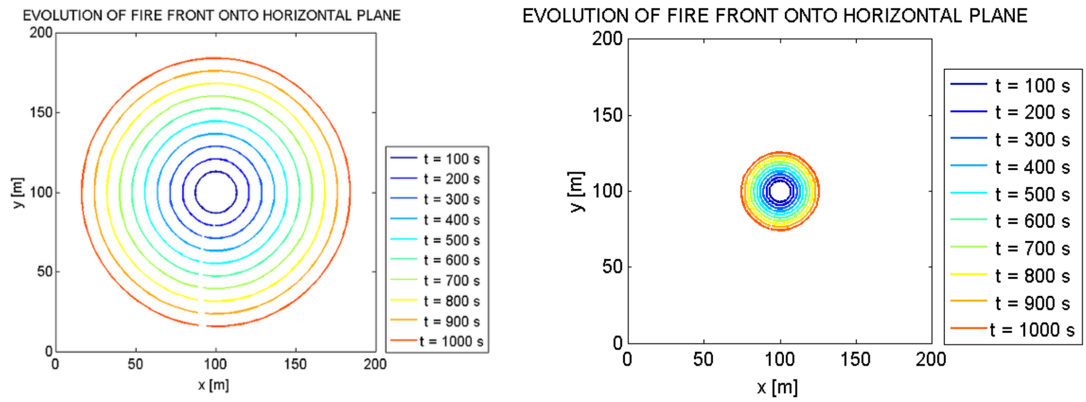

Figure 38: Fire front evolution over a 1000-s time period for an isotropic case starting from a circular initial condition; case with no wind and flat terrain corresponding to case A1a (see Section 3.2.5). Left: Balbi. Right: Rothermel.

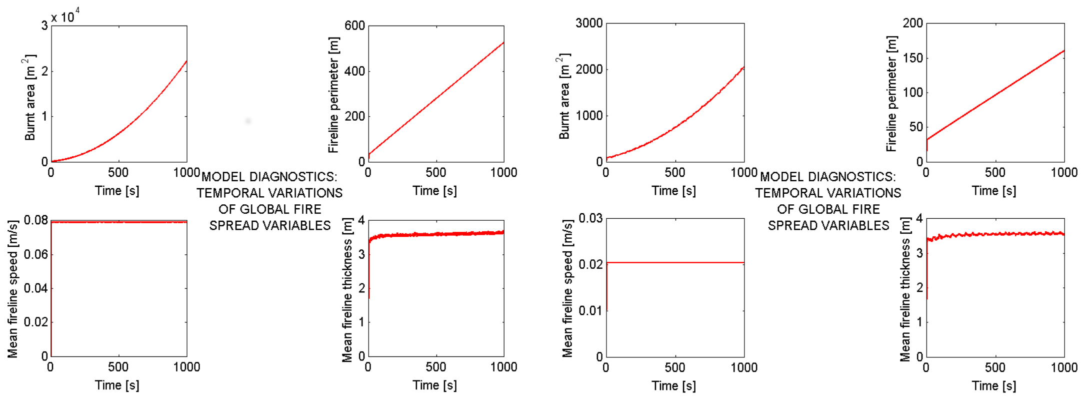

Figure 39: Model diagnostics corresponding to Fig. 38: temporal variations of global fire spread variables (burnt area, fireline perimeter, mean ROS along the fireline, mean fireline thickness) for Balbi's ROS formulation (left) and Rothermel's ROS formulation (right).

circular initial case (corresponding to the B1b case in Rochoux 2014b). In this context, the wind is uniform, with a northerly, 0.75-m/s wind. It is thus quiet straight forward to analyse case B1b. Figure 40 shows the successive fireline positions for the Balbi's ROS formulation on the left panel and for the Rothermel's ROS formulation on the right panel. It is also found that the ROS is more important with Balbi's formulation than with Rothermel's formulation. The fire front propagates faster against the wind with Balbi's ROS, too. The shape of the fireline is also different in both cases, Balbi's formulation induces a sharp head of the front while Rothermel's formulation shows a flat shape for the head front. Figure 41 presents the counterpart of Fig. 39 for the case B1b. A sharp transition is observed in Balbi's simulation results after 400 s due to fireline arrival at the limits of the burn field (the fire stops propagating in this area).

Test case B3 (see Section 3.2.5) features a non-uniform wind (see Fig. 17), it is thus harder to analyse. Still Balbi's ROS value is again larger than Rothermel's, thus resulting in a faster propagation of the front as illustrated in figure 42. It should be noted that Balbi's fronts are sharper than those simulated with Rothermel.

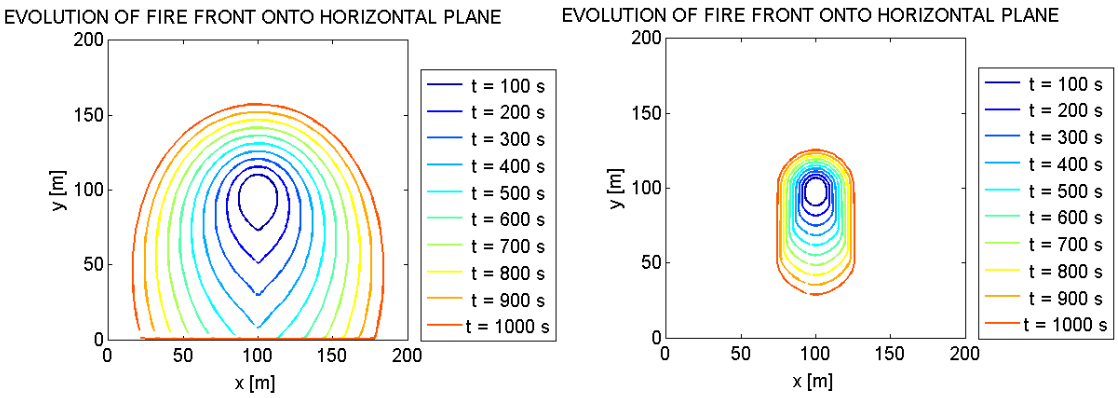

Figure 40: Fire front evolution over a 1000-s time period for an isotropic case starting from a circular initial condition; case with a uniform, northerly wind and flat terrain corresponding to case B1b (in FireFly's technical documentation). Left: Balbi. Right: Rothermel.

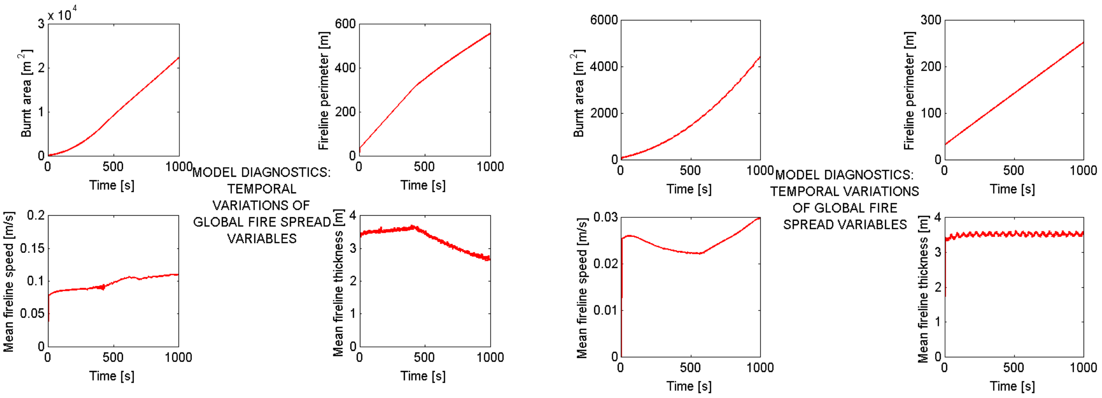

Figure 41: Model diagnostics corresponding to Fig. 40: temporal variations of global fire spread variables (burnt area, fireline perimeter, mean ROS along the fireline, mean fireline thickness) for Balbi's ROS formulation (left) and Rothermel's ROS formulation (right).

4.2.3 ROS problem encountered

Figure 43 shows the spatial distribution of the ROS at time 400 s for Balbi's formulation on the left panel and for Rothermel's formulation on the right panel for the B1b test case. The ROS values computed with Rothermel are coherent with Eq. (4), the fire propagates faster in the wind direction (with the maximum value at the head of the front) while the back of the fire propagates at the no-wind ROS. This results in a sharp description of the ROS. In contrast, Balbi's formulation results in a smoother ROS field with a uniformly varying impact of the wind direction along the fire front. The ROS is still at a maximum for the head of the front and at a minimum at the back of the front. It should be noted that some markers at the head of front display a relatively large ROS value in Balbi's case, (further investigated). While this issue should be further investigated, the numerical scheme in the level-set solver tends to filter out this peak values so that the propagated front are smooth.

The ROS extreme value in Balbi's case might be due to a time step problem. In order to validate/invalidate this hypothesis, time step was decreased from 0.5 s to

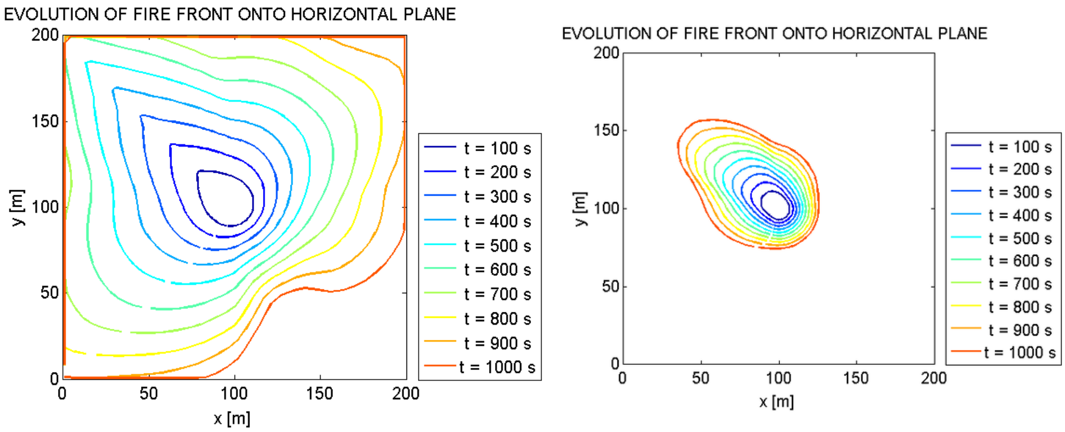

Figure 42: Fire front evolution over a 1000-s time period for an anisotropic case starting from a circular initial condition; case with a spatially-distributed, northerly wind and flat terrain corresponding to case B3 (see section 3.2.5). Left: Balbi. Right: Rothermel.

0.05 s. Fig. 44 shows the ROS obtained for each front marker, at 400 s. The red line correspond to the 0.5 s time step case, and the blue one is the 0.05 s time step case. The results are almost the same in both cases. There is the same extreme value for the first front marker at 400 s for both time steps. To conclude, this value is not due to the time step. Another hypothesis is that the extreme and local ROS value in Balbi's formulation are due to numerical issue in the normal direction identification for each marker. This still needs to be looked into details but goes beyond the scope of the present study.

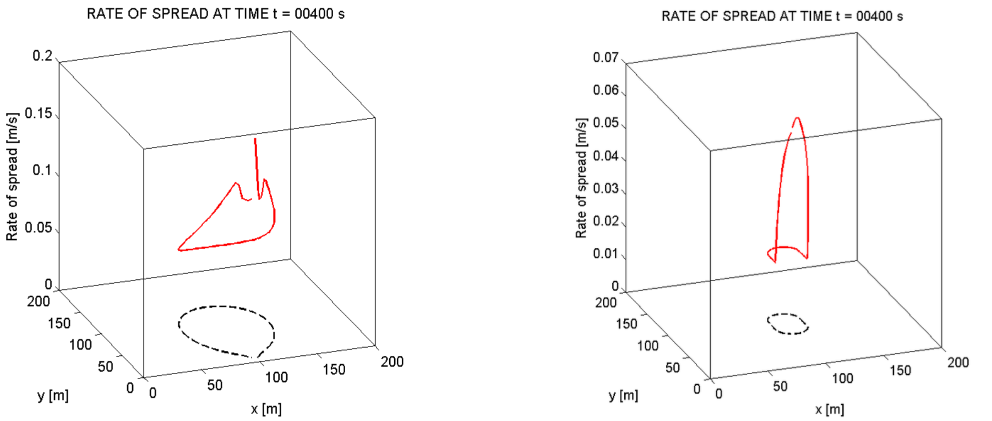

Figure 43: Spatial distribution of the ROS along the simulated fireline at time 400 s for Balbi's formulation (left) and Rothermel's formulation (right). The red line corresponds to the ROS along the fireline; and the black dashed line corresponds to the fire front location on the horizontal plane.

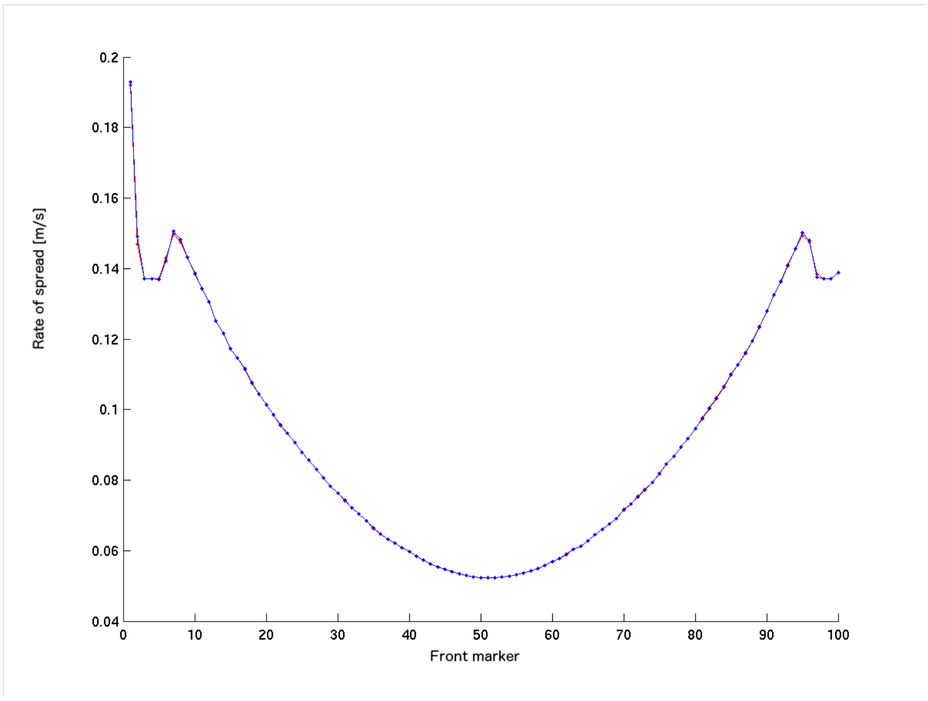

Figure 44: ROS value for each front marker at time: 400 s for B1b case. Red line: with a 0.5 s time step, blue line: with a 0.05 s time step.

4.3 Comparison on the case FireFlux

In order to validate the FireFly implementation on a larger controlled burn, the code was adapted to the FireFlux experiment. This experiment differs from the other test cases and the input data are not easily traduced within the Firefly input files. For this test case, the field is larger, the wind is uniform (set 1.46 m/s), the terrain is flat and the biomass correspond to a tall uniform grass (for more details see Section 3.3). Figure 45 shows the evolution of the front location over a 1000-s time simulation period. The two models agree with regards to the direction of the fireline. Still, considering results form previously illustrated test cases, it is expected that the Balbi ROS value be stronger than Rothermel's; which is suprisingly not observed here.

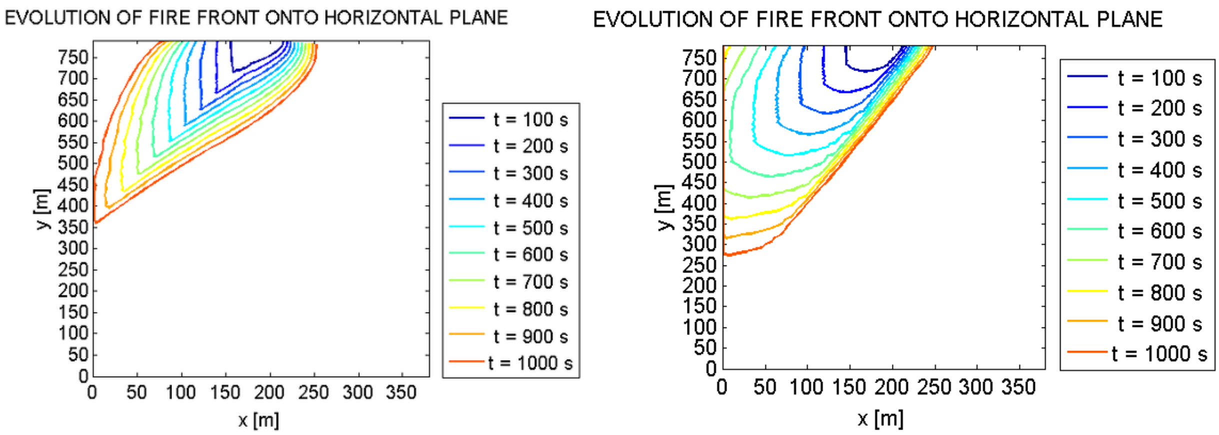

Figure 45: Evolution of the front location during the FireFlux simulation. Right: Balbi. Left: Rothermel.

Both simulations are than compared to ForeFire simulated fire fronts that is taken as a reference simulation as front locations where not observed in the real FireFlux experiment. Rothermel's simulated fronts displayed in Fig. 46 propagate significantly slower than ForeFire pseudo-observations; especially on the flank of the fire. This suggests that the description of the input data is not complex enough or that the FireFly model does not include enough physics to represent the FireFlux test case as of today. Balbi's fronts are even slower, which is not expected. As the ROS differences between Balbl are due to the sub-models implementation, it is possible that empirical parameters should be further adjusted in the future. Further investigations on the setting of the data are needed for Balbi's case to be more realistic.

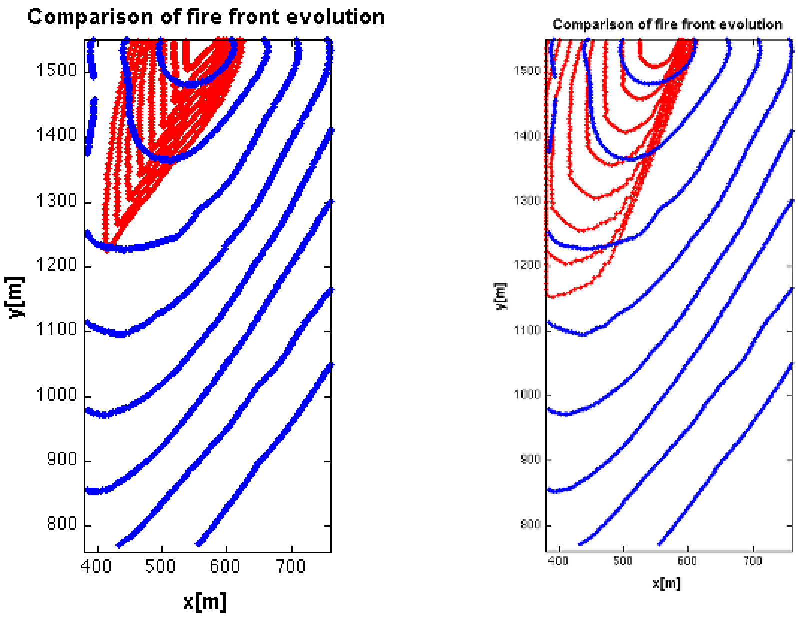

Figure 46: Comparison between the ForeFire simulation (blue) and the FireFly simulation (red). Right: Balbi. Left: Rothermel.

5 Conclusion

While much progress has been achieved over the past few decades in the basic understanding of wildfire dynamics, while also much progress has been achieved in the mathematical formulation and numerical simulation of wildfire spread, forecasting reliable scenarios of wildfire spread at an operational level remains a challenging task because the problem involves both multi-physics and multi-scales. The aim of the present work was to compare two physical representations of wildfire spread at a regional scale, that is the scale used in an operational framework. In the first part of this project, a physical approach to the wildfire spread was presented, with the two physical representations of the fire front used in this project, namely Balbi's and Rothermel's ROS models, the assumptions made and the underlying equations. The working of the wildfire spread model, and its computation of the problem is also presented. The second part of this report provides an overview of the tools and experimental settings used for this project, namely the model coupler OpenPALM, the FireFly architecture and the technical implementation used to solve this problem, as well as the FireFlux experiment used to validate the FireFly spread model on a larger experiment than previously. The third part presents the result of the comparaison of the two ROS models in the implemented models: first, a sensitivity study on the input parameters of both models, performed on a simplified model, and then the implementation in FireFly. This present work still needs to be continued because Balbi's formulation was partly hardcoded, and thus some submodels need to be coded in order to implement Balbi's formulation in the data-driven version of FireFly. Moreover, there lies a non physical value of ROS is obtained at the head of the firefront with Balbi's ROS, and the investigations led were not successful to explain it.

As a conclusion to the comparative study of both ROS models, there are significant differences in the impact of the input parameters according to the chosen physical representation of the fireline. Another difference between both models relates the mean speed of the fire front: Balbi's front propagates faster than Rothermel's one, this can be seen in the simplified model as well as in the FireFlux simulation.

While fire spread forecast capabilities are still at an early stage of development, it is envisioned that they will be similar to current weather forecasting capabilities and that the general ability to predict the evolution of wildfires will rely on the continuous assimilation of remote sensing observations into a multi-physics fire model (accounting for fire surface propagation and atmospheric dynamics). It is also envisioned that these future capabilities for forecasting wildfire spread scenarios will not uniquely rely on an unique spread-rate model but instead on a variety of spread-rate models that are characterized by different validity ranges and whose prediction capacity can thereby vary for different fire regimes.

A Diagramme de Gantt

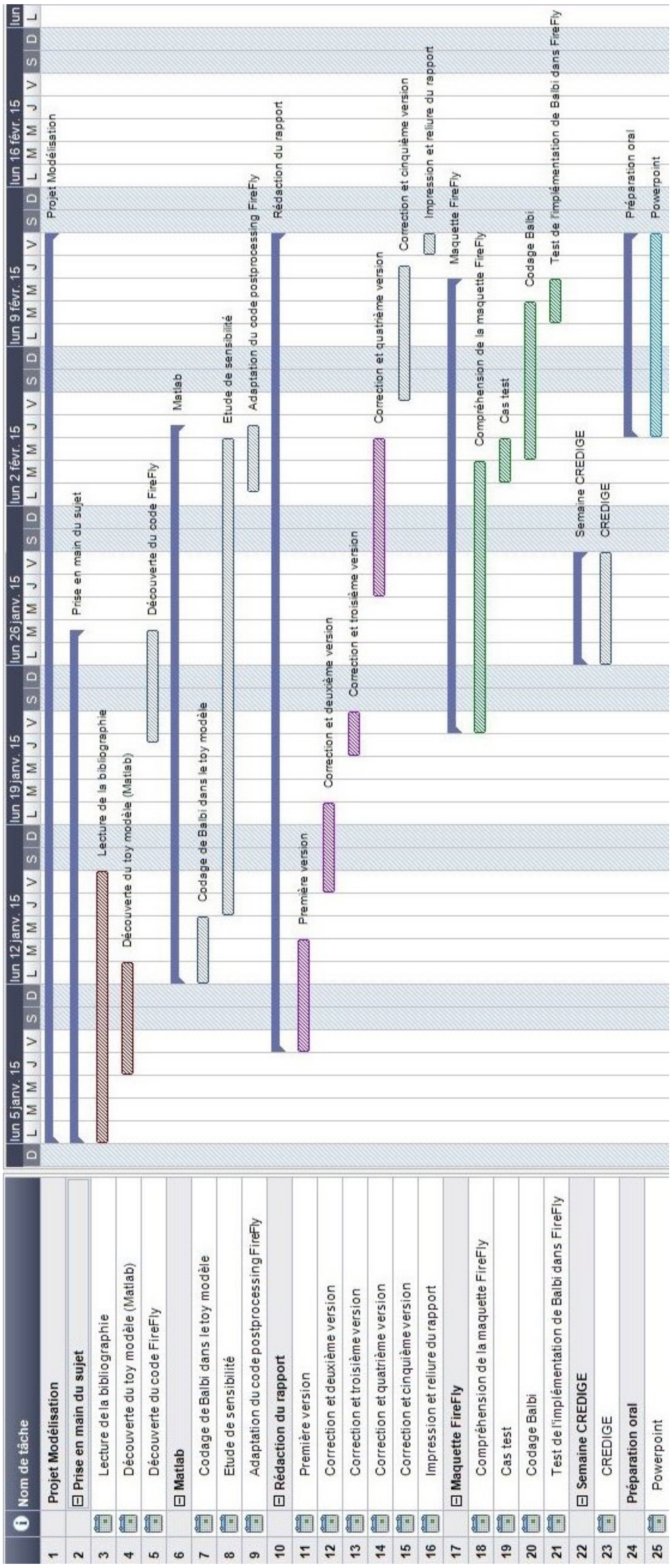

B FireFly architecture

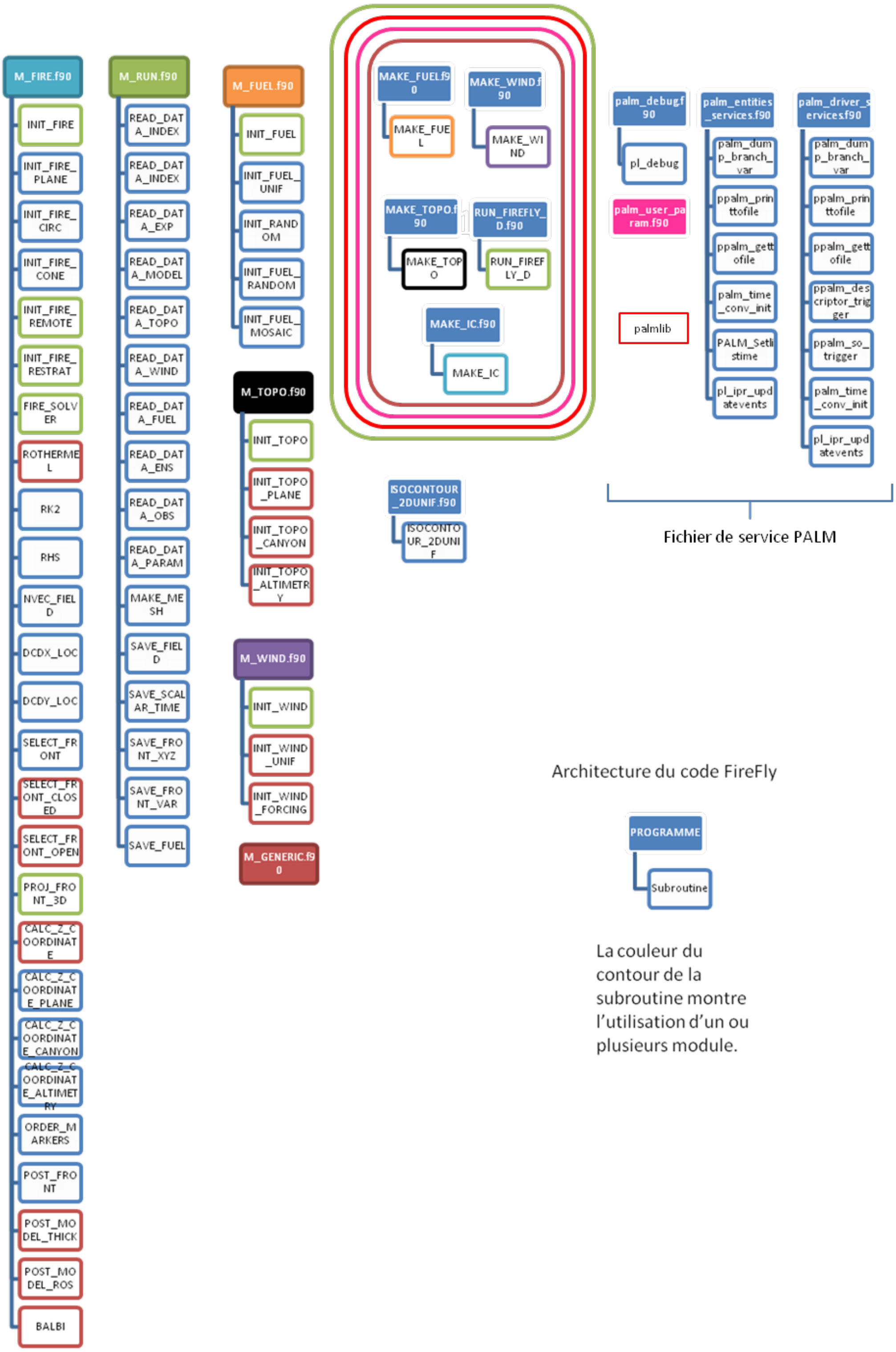

C Subroutine BALBI Fortran

```
SUBROUTINE BALBI ( &
  nfr_x,   & !normal direction to fire front: x-component (IN)
  nfr_y,   & !normal direction to fire front: y-component (IN)
  nwind,   & !number of wind parameters (IN)
  pwind,   & !wind parameters (IN)
  ntopo,   & !number of terrain topography parameters (IN)
  ptopo,   & !topography parameters (IN)
  nfuel,   & !number of biomass fuel parameters (IN)
  pfuel,   & !biomass fuel parameters (IN)
  ros_ref, & !local value of rate of spread (OUT)
  fi_ref   & !local value of the fireline intensity (OUT)
  )

!-- MODULES
  USE M_GENERIC


!-- ARGUMENTS
  !- in
  INTEGER, INTENT(IN) :: nwind, ntopo, nfuel
  DOUBLE PRECISION, INTENT(IN) :: nfr_x, nfr_y
  DOUBLE PRECISION, DIMENSION(nwind), INTENT(IN) :: pwind
  DOUBLE PRECISION, DIMENSION(ntopo), INTENT(IN) :: ptopo
  DOUBLE PRECISION, DIMENSION(nfuel), INTENT(IN) :: pfuel

  !- out
  DOUBLE PRECISION, INTENT(OUT) :: ros_ref
  DOUBLE PRECISION, INTENT(OUT) :: fi_ref


!-- LOCAL VARIABLES
  INTEGER :: i, j
  DOUBLE PRECISION :: uwx_si, uwy_si
  DOUBLE PRECISION :: slope, aspect, slope_rad, aspect_rad
  DOUBLE PRECISION :: idv, mv, dv_si
  DOUBLE PRECISION :: uw_mag_si, uw_fr_si
  DOUBLE PRECISION :: h_si, rhop_si
  DOUBLE PRECISION :: bv_t, uw_mag, uw_fr
  DOUBLE PRECISION :: sv_t, wn_t, rhob_t
  DOUBLE PRECISION :: proj2D
  DOUBLE PRECISION :: ros0_si, ros_si
  DOUBLE PRECISION :: rad_frac_0, nu_v, alpha_fr, temp_fr, temp_ign, temp_air, eps_fr
  DOUBLE PRECISION :: sigma_sb, cp, wn_h2o, delta_hm, ra, a_fr, dv_opt, A0, u_0, nd, w
  DOUBLE PRECISION :: dw, alpha_w, alpha_sl, u


!-- ROUTINE

  !- ENVIRONMENTAL CONDITIONS (SI UNITS) -------------------------!

  !-> wind conditions
  uwx_si = pwind(1) !x-component of the local wind velocity vector [m/s]
  uwy_si = pwind(2) !y-component of the local wind velocity vector [m/s]

  !-> terrain topography parameters
  slope = ptopo(1)  !terrain slope angle [deg]
  aspect = ptopo(2) !terrain aspect angle on horizontal plane [deg]
  slope_rad = slope*pi/180.d0 !terrain slope angle [rad]
  aspect_rad = aspect*pi/180.d0 !terrain aspect angle on horizontal plane [rad]

  !-> biomass fuel parameters
  idv = pfuel(1)     !index of fuel species
  mv = pfuel(2)      !fuel moisture content
  dv_si = pfuel(3)   !fuel layer thickness [m]



  !- TREATMENT OF WIND CONDITIONS ---------------------------------!

  !-> local wind magnitude [m/s]
  uw_mag_si = DSQRT(uwx_si**2 + uwy_si**2)

  !-> wind projected alond the normal direction to the front [m/s]
  uw_fr_si = (uwx_si*nfr_x - uwy_si*nfr_y)



  !- BIOMASS FUEL DATABASE ----------------------------------------!

  !-> common features
  h_si = 18607112.1d0  !heat of combustion [J/kg]
```

```
  rhop_si = 512.588d0  !ovendry particle density [kg/m^3]

  !-> specific features (4 models + 1 user-defined)
  IF (idv.EQ.1) THEN      !SHORT GRASS (dv_si ~ 30.5 cm)
    sv_t = 11482.94d0     !fuel particle surface-to-volume ratio [1/m]
    bv_t = 0.001063d0     !fuel packing ratio [-]
  ENDIF

  rhob_t = bv_t*rhop_si
  wn_t = rhob_t*dv_si


  !- SUBMODELS --------------------------------------------------!

  !- angles
  IF (nfr_x.GT.eps)THEN
    nd = DATAN(nfr_y/nfr_x) ! local normal direction [rad]
  ELSEIF (nfr_y .GT. eps) THEN
    nd = pi/2.d0
  ELSEIF (nfr_y .LT. eps) THEN
    nd = -pi/2.d0
  ELSE
    nd = 0.d0
  ENDIF

  IF (uwx_si.GT.eps) THEN
    dw = DATAN(uwy_si/uwx_si) ! wind direction corresponding to the direction from wich the wind is blowing
  ELSEIF (uwy_si.GT.eps) THEN
    dw = pi/2.d0
  ELSEIF (uwy_si .LT. eps) THEN
    dw = -pi/2.d0
  ELSE
    dw = 0.d0
  ENDIF
  alpha_w = dw ! wind direction angle


  !- variables and constants
  eps_fr = 0.3d0      ! flame emissivity (FireFlux)
  rad_frac_0 = 0.3d0  ! radiative fraction when the flame surface-to-volume ratio converges to zero
  u_0 = 2             ! buoyancy velocity [m/s]
  delta_hm = 2.5d4    ! moisture evaporation enthalpy [J/kg]
  cp = 2000           ! vegetal calorific capacity [J/kg]
  temp_ign = 593      ! ignition temperature [K]
  temp_air = 293      ! ambient temperature [K]
  sigma_sb = 5.67d-8  ! Stephan-Boltzmann constant [W/m^2K]
  temp_fr = 1440      ! flame temperature [K]
  A0 = 2.25           ! ratio between incident radiant and ignition energy
  dv_opt = 4/(sv_t*bv_t)           ! optimal length scale
  nu_v = MIN((dv_si/dv_opt), 1.d0) ! absorption coefficient for radiation
  wn_h2o = mv*100.d0  ! moisture content [%]

  !- wind speed along the normal direction to the front [m/s]
  w = uw_fr_si

  !- buoyancy velocity [m/s]
  u = u_0/DCOS(slope_rad)

  !- flame tilt [rad]
  alpha_fr = DATAN((w/(u*DCOS(slope_rad))) + DTAN(slope_rad))


  !- RATE OF SPREAD ---------------------------------------!

  !-> no-slope no-wind rate of spread [m/s]
  ros0_si = (eps_fr*sigma_sb*(temp_fr**4)*dv_si)/(2.d0*wn_t*(cp*(temp_ign- &
                temp_air) + wn_h2o*delta_hm))

  !-> rate of spread formulation [m/s]
  a_fr = (1.d0 + DSIN(alpha_fr) - DCOS(alpha_fr))/DCOS(alpha_fr)
  ra = ros0_si*(1.d0 - 12.d0/DCOS(alpha_fr) + (12.d0*nu_v*A0*a_fr)/ &
             (1.d0 + (wn_h2o*delta_hm)/(4.d0*cp*(temp_ign - temp_air))))
  ros_si = (1.d0/2.d0)*(ra+DSQRT((ra**2)+ (4.d0*ros0_si*12.d0*ros0_si)/(DCOS(alpha_fr))))

  !-> rate of spread projected onto two-dimensionam horizontal plane
  proj2D = 1.d0/DSQRT(1.d0 + (slope_rad**2)*(DCOS(aspect_rad)*nfr_y + DSIN(aspect_rad)*nfr_x)**2)

  !-> outputs: rate of spread (m/s), fireline intensity (kW/m)
  ros_ref = ros_si*proj2D
  fi_ref = (h_si*wn_t)*ros_ref*(1e-3)

  RETURN
END SUBROUTINE BALBI
```

D Lexicon

$c_{p,v}$	fuel calorific capacity	capacité calorifique à pression constante du combustible
H_{fr}	flame height	hauteur de flamme
I_p	propagating heat flux	flux de chaleur lié à la propagation
l	flame length	longueur de flamme
M_v	fuel moisture content	humidité du combustible
$M_{v,ext}$	fuel moisture content at extinction	humidité d'extinction du combustible
m''_n	net fuel loading	charge nette du combustible
m''_v	fuel loading	charge du combustible
$\dot{m}''_v$	vegetation mass loss rate	taux de perte de masse dans la végétation
n_m	moisture damping coefficient	coefficient d'atténuation (humidité)
n_s	mineral damping coefficient	coefficient d'atténuation (minéral)
Q_{fr}	heat release rate by combustion	taux de chaleur émis par combustion
Q_{ig}	heat of preignition	chaleur de pré-allumage
s_t	fuel particle total mineral content	contenu minéral total du combustible
s_e	fuel particle effective mineral content	contenu minéral effectif du combustible
T_{air}	ambient temperature	température de l'air ambiant
T_{ign}	temperature of ignition	température d'allumage
u_b	buoyancy velocity	vitesse de flottabilité
u_w	wind velocity at mid-flame height	vitesse du vent à la hauteur de mi-flamme
α_{fr}	flame tilt angle	angle d'inclinaison de la flamme
α_{sl}	terrain slope angle	angle de pente
β_v	fuel packing ratio	compacité de la couche de végétation
$\beta_{v,opt}$	optimal fuel packing ratio	compacité optimale
γ	reaction velocity	vitesse de réaction
γ_{max}	maximal reaction velocity	vitesse de réaction maximale
δ_{fr}	fire front depth	épaisseur du front de flamme
Δh_c	fuel low heat of combustion	chaleur de combustion
Δh_v	moisture evaporation enthalpy	chaleur de vaporisation de l'eau
δ_v	fuel depth	hauteur de la strate de végétation
$\delta_{v,opt}$	optimal length scale	libre parcours moyen du rayonnement à travers le milieu végétal
ε	effective heating number	paramètre effectif de chaleur
ε_{fr}	flame emissivity	émissivité de la flamme
ε_v	vegetation emissivity	émissivité de la végétation
Φ^*_{sl}	slope correction coefficient	coefficient de correction de la pente
Φ^*_w	wind correction coefficient	coefficient de correction du vent
χ_{rad}	radiation fraction	fraction de la chaleur de combustion rayonnée par la flamme
ρ_b	bulk mass density	masse volumique apparente
$\rho_b\varepsilon$	effective fuel density	masse volumique effective
ρ_p	fuel particle mass density	masse volumique du combustible
Σ_v	fuel surface to volume ratio	rapport de la surface de la particule de combustible sur son volume

E Fonction BALBI Matlab

```
function sol = fct_balbi_eval_2D(lv, mv, dv, sv, h, rhop, w, ...
    alpha_fr, alpha_w, alpha_a, alpha_sl)

%************************************************************
% ARGUMENTS
% -IN
%   -lv: fuel surface loading [kg/m2]
%   -mv: moisture content [-]
%   -dv: fuel layer thickness [m]
%   -sv: fuel particle surface-to-volume ratio [1/m]
%   -h: heat of combustion [J/kg]
%   -rhop: fuel particle mass density [kg/m3]
%   -w: wind speed at mid-flame height [ft/min]
%   -alpha_fr: local normal direction [rad]
%   -alpha_w: blowing wind direction [rad]
%   -alpha_a: aspect angle direction [rad]
%   -sl: vertical rise divided by horizontal distance [rad]
%
% -OUT
%   -sol: vector of length 2 for the rate of spread (ROS) values
%         1- no-wind no-slope ROS
%         2- wind-aided and slope-aided ROS
%************************************************************

%-------------------------------------------------------------------------
% MODEL PARAMETERS



emis = 0.3;                 % flame emissivity
chi0 = 0.3;                 % radiative fraction
u0 = 2;                     % buoyancy velocity [m/s]
dhv = 2.5e4;                % moisture evaporation enthalpy [J/kg]
cp = 2000;                  % vegetal calorific capacity [J/kg]
rho = 0.25;                 % flame gas density [kg/m3]
s = 9;                      % stoichiometric coefficient
Ti = 593;                   % ignition temperature [K]
Ta = 293;                   % ambient temperature [K]
B = 5.67e-8;                % Stephan-Boltzmann constant [W/m^2K]
T = 1440;                   % flame temperature [K]
Ao = 2.25;                  % ratio between incident radiant and igntion energy
rhob = lv/dv;               % fuel bulk density [kg/m3]
bv = rhob/rhop;             % fuel layer packing ratio [-]
delta = 4/(sv*bv);          % optical length scale
nu = min((dv/delta),1);     % absorption coefficient for radiation

%disp(min((dv/delta),1))

mv = mv*100;                % moisture content [%]
%-------------------------------------------------------------------------
% SUBMODELS
% Ao
%Ao = (chi0*dhv)/(4*cp*(Ti-Ta));

%- 2D effect
w = w*max(0,cos(alpha_fr - (alpha_w + pi)));

%- buoyancy velocity [m/s]
u = u0/cosd(alpha_sl);

%- flame tilt
%--- in rad
gamma0 = atan((w/(u*cosd(alpha_sl))) + tand(alpha_sl));
%--- in deg
gamma = radtodeg(gamma0);


%- no-wind no-slope rate of spread
ros0 = (emis*B*(T^4)*dv)/(2*lv*(cp*(Ti-Ta) + mv*dhv));


%- rate of spread formulation [m/s]
A_fr=(1+sind(gamma)-cosd(gamma))/cosd(gamma);
 Ra = ros0 - (12*ros0)/cosd(gamma) + (Ao*nu)/(1+((mv*dhv)/(4*cp*(Ti-Ta)))) ...
     * ((1+sind(gamma)-cosd(gamma))/cosd(gamma))*(12*ros0);
%Ra = ros0 - (12*ros0)/cosd(gamma) + (12*ros0*nu*chi0*h)/(4*cp*(Ti-Ta) ...
%    + mv*dhv) * ((1+sind(gamma)-cosd(gamma))/cosd(gamma));

ros_balbi = (Ra + sqrt(Ra^2 + (4*ros0*(12*ros0))/cosd(gamma)))/2;

```

```
disp(ros_balbi)

%- output solution
sol = [ros0 ros_balbi];

return;
```

List of Figures

List of Tables

References

C. Ashton, G. Rein, J.D. Rivera, J.L. Torero, C. Leff, M. Davies, and A. Gray. Experiments and observations of peat smouldering fires. In *International Meeting of Fire Effects on Soil Properties*, Barcelona, 2007.

J.-H. Balbi, F. Morandini, X. Silvani, J.-B. Filippi, and F. Rinieri. A physical model for wildland fires. *Combustion and Flame*, 156(12):2217–2230, December 2009. ISSN 00102180. doi: 10.1016/j.combustflame.2009.07.010. URL http://linkinghub.elsevier.com/retrieve/pii/S0010218009001989.

N. Cheney, J. Gould, and W. Catchpole. Prediction of fire spread in grasslands. *International Journal of Wildland Fire*, 8(1):1–13, 1998.

C.B. Clements. Fireflux - Observing wildland grass fire dynamics. *Bulletin of the American Meteorological Society*, 88(9):1369–1382, 2007.

J.-B. Filippi, F. Bosseur, C. Mari, C. Lac, P. Le Moigne, B. Cuenot, D. Veynante, D. Cariolle, and J.-H. Balbi. Coupled atmosphere-wildland fire modelling. *Journal of Advances in Modeling Earth Systems*, 1(4):Quarter 4, 2009.

J.-B. Filippi, X. Pialat, and C.B. Clements. Assessment of ForeFire/Meso-NH for wildland fire/atmosphere coupled simulation of the FireFlux experiment. *Proceedings of the Combustion Institute*, 34:2633–2640, 2013.

W. Fons. Analysis of fire spread in light forest fuels. *Journal of Agricultural Research*, 72:93–121, 1946.

W Frandsen. Fire spread through porous fuels from the conservation of energy. *Combustion and Flame*, 16:9–16, 1971.

A. Grishin. Mathematical modeling of forest fires and new methods of fighting them. Technical report, Publishing House of Tomsk State University, English translation edition, Tomsk, Russia, 1997.

R.M. Hadden, G. Rein, and C.M. Belcher. Study of the competing chemical reactions in the initiation and spread of smouldering combustion in peat. *Proceedings of the Combustion Institute*, 34:2547–2553, 2013.

H.P. Hanson, M.M. Bradley, J.E. Bossert, R.R. Linn, and L.W. Younker. The potential and promise of physics-based wildfire simulation. *Environmental Science and Policy*, 3: 161–172, 2000.

A.K. Kochanski, M.A. Jenkins, J. Mandel, J.D. Beezley, and S.K. Krueger. Real time simulation of 2007 Santa Ana fires. *Forest Ecology and Management*, 294:136–149, 2013. ISSN 0378-1127. doi: 10.1016/j.foreco.2012.12.014. URL http://dx.doi.org/10.1016/j.foreco.2012.12.014.

T. Lagarde, A. Piacentini, and O. Thual. A new representation of data assimilation methods: The PALM flow charting approach. *Quarterly Journal of the Royal Meteorological Society*, 127:189–207, 2001.

M. Larini, F. Giroud, B. Porterie, and J.C. Loraud. A multiphase formulation for fire propagation in heterogeneous combustible media. *International Journal of Heat and Mass Transfer*, 41(6-7):881–897, 1998.

R. Linn, J. Reisner, J.J. Colman, and J. Winterkamp. Studying wildfire behavior using FIRETEC. *International Journal of Wildland Fire*, 11:233–246, 2002.

D. Morvan and J.L. Dupuy. Modeling the propagation of a wildfire through a Mediterranean shrub using a multiphase formulation. *Combustion and Flame*, 138:199–210, 2004.

B. Porterie, J.L. Consalvi, A. Kaiss, and J.C. Loraud. Predicting wildland fire behavior and emissions using a fine-scale physical model. *Numerical Heat Transfer: Part A: Applications*, 47(6):571–591, 2005.

R. Rehm and R. McDermott. Fire front propagation using the level set method. Technical Report March, National Institute of Standards and Technology, 2009.

M. Rochoux. *Vers une meilleure prévision de la propagation d'incendies de forêt : évaluation de modèles et assimilation de données*. PhD thesis, École Centrale Paris, France, 2014a.

M. Rochoux. *Firefly, Technical reference, Firefly a regional-scale data-driven wildfire spread simulator.*, 2014b. URL http://sophiericci.neowordpress.fr/.

R.C. Rothermel. A mathematical model for predicting fire spread in wildland fuels. Technical report, U.S. Department of Agriculture, Forest Service, Intermountain forest and range experiment station, Ogden, Utah, USA, 1972.

A.L. Sullivan. Wildland surface fire spread modeling, 1990-2007. 2: Empirical and quasi-empirical models. *International Journal of Wildland Fire*, 18:369–386, 2009.

E.F. Toro. *Reimann solvers and numerical methods for fluid dynamics: A practical introduction*. Springer, second edition, 1999.

D.X. Viegas. Forest Fire Propagation. *Philosophical Transactions: Mathematical, Physical and Engineering Sciences*, 356:2907–2928, 1998.

D.X. Viegas. Overview of forest fire propagation research. *Proceedings of the International Association of Fire Safety Science*, 10:95–108, 2011.

F. Williams. Urban and wildland fire phenomenology. *Progress in Energy and Combustion Science*, 8:317–354, 1982.